Synapse and active zone assembly in the absence of presynaptic Ca2+ channels and Ca2+ entry

Held, R.G.; Liu, C.L.; Ma, K.P.; Ramsey, A.M.; Tarr, T.B.; Nola, G. de; ... ; Kaeser, P.S.

Neuron

CellPress

Article

Synapse and Active Zone Assembly in the Absence of Presynaptic Ca^{2+} Channels and Ca^{2+} Entry

Richard G. Held,[1,6,7] Changliang Liu,[1,6] Kunpeng Ma,[1,2,6] Austin M. Ramsey,[3] Tyler B. Tarr,[3] Giovanni De Nola,[1] Shan Shan H. Wang,[1] Jiexin Wang,[1] Arn M.J.M. van den Maagdenberg,[4] Toni Schneider,[5] Jianyuan Sun,[2] Thomas A. Blanpied,[3] and Pascal S. Kaeser[1,8,*]

[1]Department of Neurobiology, Harvard Medical School, Boston, MA 02115, USA
[2]State Key Laboratory of Brain and Cognitive Sciences, Institute of Biophysics, Chinese Academy of Sciences, and University of Chinese Academy of Sciences, Beijing 100101, China
[3]Department of Physiology and Program in Neuroscience, University of Maryland School of Medicine, Baltimore, MD 21201, USA
[4]Departments of Human Genetics and Neurology, Leiden University Medical Center, 2333 ZA Leiden, the Netherlands
[5]Institute for Neurophysiology, University of Cologne, Köln 50931, Germany
[6]These authors contributed equally
[7]Present address: Department of Molecular and Cellular Physiology, Stanford University, Stanford, CA 94305, USA
[8]Lead Contact
*Correspondence: kaeser@hms.harvard.edu
https://doi.org/10.1016/j.neuron.2020.05.032

SUMMARY

Presynaptic Ca_V2 channels are essential for Ca^{2+}-triggered exocytosis. In addition, there are two competing models for their roles in synapse structure. First, Ca^{2+} channels or Ca^{2+} entry may control synapse assembly. Second, active zone proteins may scaffold Ca_V2s to presynaptic release sites, and synapse structure is Ca_V2 independent. Here, we ablated all three Ca_V2s using conditional knockout in cultured hippocampal neurons or at the calyx of Held, which abolished evoked exocytosis. Compellingly, synapse and active zone structure, vesicle docking, and transsynaptic nano-organization were unimpaired. Similarly, long-term blockade of action potentials and Ca^{2+} entry did not disrupt active zone assembly. Although Ca_V2 knockout impaired the localization of β subunits, α2δ-1 localized normally. Rescue with Ca_V2 restored exocytosis, and Ca_V2 active zone targeting depended on the intracellular C-terminus. We conclude that synapse assembly is independent of Ca_V2s or Ca^{2+} entry through them. Instead, active zone proteins recruit and anchor Ca_V2s via Ca_V2 C-termini.

INTRODUCTION

Ca^{2+} channels are concentrated in the presynaptic plasma membrane at sites for exocytosis called active zones (Eggermann et al., 2011; Kaeser and Regehr, 2014; Simms and Zamponi, 2014; Südhof, 2012). Ca^{2+} entry through Ca_V2 channels triggers synaptic vesicle release. Synaptic strength, speed, and plasticity—hallmark features of synaptic transmission—rely on the precise positioning of Ca^{2+} channels within 10–200 nm of release-ready vesicles such that Ca^{2+} rises and falls quickly during an action potential at the vesicular Ca^{2+} sensor (Bucurenciu et al., 2008; Kaeser et al., 2011; Nakamura et al., 2015). Given the importance of these spatial relationships, understanding the mechanisms and roles of Ca^{2+} channels in the assembly of release sites and synapses is essential. Previous work on the organization and targeting mechanisms of Ca^{2+} channels (Cao et al., 2004; Chen et al., 2011; Hibino et al., 2002; Kaeser et al., 2011; Lübbert et al., 2019; Nishimune et al., 2004; Rebola et al., 2019; Schneider et al., 2015) can be broadly summarized in two models. In the first, Ca^{2+} channels or Ca^{2+} entry controls the scaffolding of the active zone and other synaptic proteins, thus guiding synapse organization ("Ca_V2-driven assembly model"). In the second, active zone or other synaptic proteins provide the scaffolds for synapse structure, and Ca^{2+} channels are anchored by these scaffolds ("anchored Ca_V2 model").

Ca_V2-driven assembly of release sites around the channel complex would ensure proximity between the Ca^{2+} sources and sensors, and several lines of work favor this model. Ca^{2+} channels interact with proteins in the synaptic cleft and may contribute to active zone assembly at the neuromuscular junction (Chen et al., 2011; Kushibiki et al., 2019; Nishimune et al., 2004). The channels bind *in vitro* to synaptic vesicles, potentially accounting for vesicle tethering and docking (Gardezi et al., 2016; Lübbert et al., 2017; Snidal et al., 2018). Furthermore, Ca^{2+} channel sequences that bind to the active zone proteins RIM and RIM-BP (Hibino et al., 2002; Kaeser et al., 2011) boost the assembly of liquid-phase condensates of these proteins *in vitro* (Wu et al., 2019), and Ca_V2 overexpression at the calyx of Held or hippocampal synapses enhances synaptic strength and increases active zone size (Heck et al., 2019; Lübbert

et al., 2019; Schneider et al., 2015). Moreover, at inner hair cell and retinal ribbon synapses, where Ca_V1s mediate release, Ca^{2+} channel ablation leads to defects in synapse and active zone structure and maintenance (Kerov et al., 2018; Sheets et al., 2012). α2δ subunits, which are important for Ca^{2+} channel trafficking, may also control synapse structure at hippocampal synapses (Hoppa et al., 2012; Schneider et al., 2015), the end-bulb of Held (Pirone et al., 2014), ribbon synapses (Fell et al., 2016; Kerov et al., 2018; Wang et al., 2017), and independently of the pore-forming subunit at the fly neuromuscular junction (Kurshan et al., 2009). In summary, roles of the Ca_V2 complex may include the control of nerve terminal and active zone size, Ca^{2+} channel abundance, and the alignment of active zones with postsynaptic densities.

In the anchored Ca_V2 model, the active zone recruits Ca^{2+} channels and targets them with nanoscale precision to release sites, and hence synapse structure is Ca_V2 independent. Support for this model comes from mouse knockout studies of active zone proteins, for example of RIM, RIM-BP, or ELKS, in which their ablation leads to defects in Ca^{2+} channel localization and Ca^{2+} entry (Acuna et al., 2016; Han et al., 2011; Held et al., 2016; Kaeser et al., 2011; Kittel et al., 2006; Liu et al., 2011, 2014; Wang et al., 2016). Furthermore, overexpression of specific types of Ca^{2+} channels outcompetes endogenous channels at active zones of hippocampal synapses (Cao et al., 2004; Hoppa et al., 2012; Schneider et al., 2015), indicating that there is a limited number of sites for channel anchoring (Cao et al., 2004).

Ca^{2+} channels are complex multiprotein structures consisting of a single pore-forming α1 subunit, an intracellular β subunit, and an extracellular α2δ protein (Catterall, 2011; Witcher et al., 1993, 1995). The α1 proteins are encoded by 10 Ca_V genes of the Ca_V1–Ca_V3 families. At central synapses, neurotransmitter release is almost exclusively mediated by Ca_V2s (Cao et al., 2004; Catterall, 2011; Dietrich et al., 2003; Luebke et al., 1993; Takahashi and Momiyama, 1993), defined by three Ca_V2 α1 subunits: $Ca_V2.1$ (*Cacna1a*, P/Q-type), $Ca_V2.2$ (*Cacna1b*, N-type), and $Ca_V2.3$ (*Cacna1e*, R-type). We here use "Ca_V2" to refer to both the pore-forming α1 subunits and the corresponding channel complex. $Ca_V2.1$ and 2.2 redundantly account for the majority of release from glutamatergic hippocampal synapses, and $Ca_V2.2$ dominates early in development, while the contribution of $Ca_V2.1$ increases over time (Cao et al., 2004; Scholz and Miller, 1995). $Ca_V2.3$ channels are primarily postsynaptic but also contribute to synaptic vesicle fusion and presynaptic plasticity at central synapses (Dietrich et al., 2003; Myoga and Regehr, 2011; Wu et al., 1998). β subunits (encoded by four genes: *Cacnb1* to *Cacnb4*) and α2δ proteins (encoded by four genes: *Cacna2d1* to *Cacna2d4*) are important for Ca_V2 surface trafficking, to regulate Ca_V2 functions, and to expand the protein interaction repertoire (Cantí et al., 2005; Catterall, 2011; Ferron et al., 2018; Hoppa et al., 2012; De Waard et al., 1994).

Both the Ca_V2-driven assembly and anchored Ca_V2 models rely on Ca^{2+} channel interactions with active zone proteins. RIM PDZ domains bind to channel C-termini, and RIM-BPs interact via their SH3 domains with short proline-rich motifs of Ca^{2+} channels and RIMs, forming a tripartite complex (Hibino et al., 2002; Kaeser et al., 2011; Wu et al., 2019). Mint and CASK proteins bind to the channel C-terminus in similar ways (Maximov and Bezprozvanny, 2002). RIMs and ELKS also interact with Ca_Vβ subunits (Kiyonaka et al., 2007, 2012).

We here distinguish between the Ca_V2-driven assembly and anchored Ca_V2 models by assessing synapse structure after genetic ablation of $Ca_V2.1$, $Ca_V2.2$, and $Ca_V2.3$ or chronic blockade of Ca^{2+} entry. We find that Ca_V2s, Ca^{2+} entry through them, and Ca^{2+}-triggered exocytosis do not have essential roles in synapse structure in cultured hippocampal neurons and at the calyx of Held. Different from β subunits, α2δ-1 proteins are broadly distributed within nerve terminals, and their localization does not depend on the presence of α1. Finally, the intracellular C-terminus is important for active zone localization of Ca_V2s, with prominent roles for RIM and RIM-BP interaction sites. We conclude that Ca_V2s are not necessary for synapse structure but are recruited and targeted to the active zone by specific interactions with active zone proteins.

RESULTS

Ca_V2 Channels Are Essential for Action Potential-Triggered Release but Not Synaptic Ultrastructure

To assess Ca_V2 contributions to synapse assembly and function, we generated mice for simultaneous ablation of all three Ca_V2s. "Floxed" alleles for the conditional ablation of $Ca_V2.1$ or $Ca_V2.3$ (referred to as conditional $Ca_V2.1$- or $Ca_V2.3$-knockout mice) were previously generated (Pereverzev et al., 2002; Todorov et al., 2006), and $Ca_V2.2$ conditional knockout (cKO) mice were newly generated (Figures S1A–S1F). The mice were intercrossed to generate "triple floxed" mice in which $Ca_V2.1$, $Ca_V2.2$, and $Ca_V2.3$ can be removed by expression of cre recombinase (Figure 1A). We cultured hippocampal neurons as previously described (de Jong et al., 2018; Wang et al., 2016) and infected them with lentiviruses expressing cre recombinase (to generate Ca_V2 conditional triple-KO [cTKO] neurons) or lentiviruses expressing a truncated, inactive version of cre (to generate Ca_V2 control neurons). Surprisingly, ablating all Ca_V2 channels did not impair dendritic arborization and synapse density in these neurons (Figures 1B–1E).

We used whole-cell recordings to assess synaptic transmission in Ca_V2 cTKO neurons. Excitatory postsynaptic currents (EPSCs; measured as AMPA or NMDA receptor currents) and inhibitory postsynaptic currents (IPSCs) in response to a single stimulus or brief trains were dramatically impaired (Figures 1F–1K, S1G, and S1H), indicating that synchronous release necessitates Ca_V2s and that Ca_V1 or Ca_V3 channels do not compensate for their loss. Furthermore, the frequencies of spontaneous miniature EPSCs (mEPSCs; measured in tetrodotoxin [TTX]) and miniature IPSCs (mIPSCs) were decreased, but mEPSC amplitudes were normal (Figures 1L, 1M, and S1I–S1K).

To assess roles of Ca_V2s in synapse ultrastructure, we quantified transmission electron microscopic images of neurons fixed by high-pressure freezing followed by freeze substitution. In three-dimensional (3D) reconstructions (Figures 2A–2D) or single sections (Figures S2A–S2C), Ca_V2 cTKO synapses were indistinguishable from Ca_V2 controls in all measured parameters. Of particular note, vesicle distribution and the number of docked vesicles (defined as vesicles with no detectable separation

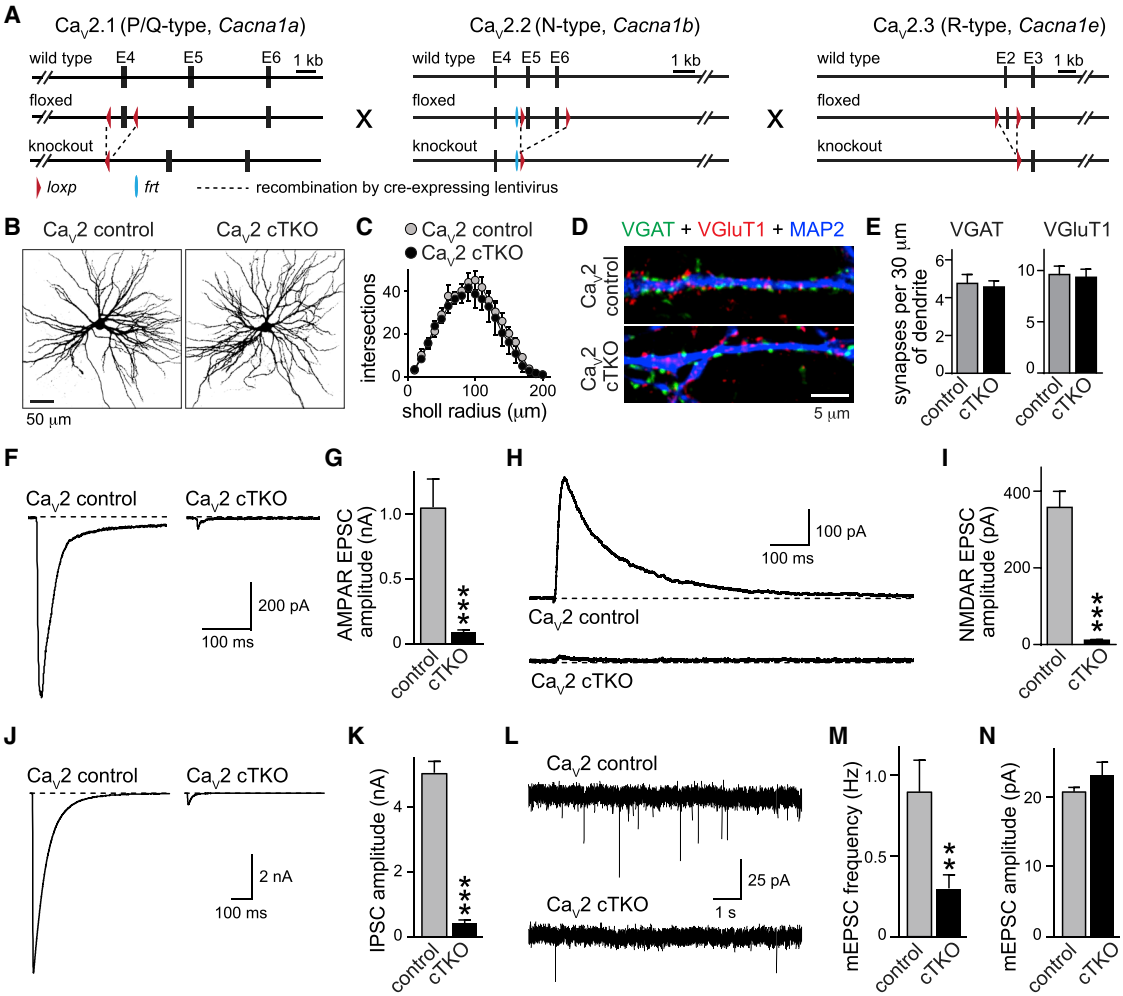

Figure 1. Ca$_V$2s Are Essential for Action Potential-Triggered Release

(A) Strategy for Ca$_V$2 α1 triple knockout in cultured hippocampal neurons.

(B and C) Binary images (B) and Sholl analysis (C) of neurons filled with Alexa 594 (Ca$_V$2 control, n = 7 cells/3 independent cultures; Ca$_V$2 cTKO n = 9/3).

(D and E) Sample images (D) and quantification (E) of densities of excitatory (VGluT1) and inhibitory (VGAT) terminals along dendrites marked by MAP2 (Ca$_V$2 control, n = 50 images/5 independent cultures; Ca$_V$2 cTKO, n = 50/5)

(F–K) Representative traces (F, H, and J) and quantification (G, I, and K) of evoked postsynaptic currents (PSCs) mediated by AMPA receptors (F and G, recorded in 1 mM γ-DGG; Ca$_V$2 control, n = 16/3; Ca$_V$2 cTKO, n = 15/3), NMDA receptors (H and I; Ca$_V$2 control, n = 13/3; Ca$_V$2 cTKO, n = 12/3), or GABA$_A$ receptors (J and K; Ca$_V$2 control, n = 20/4; Ca$_V$2 cTKO, n = 22/4).

(L–N) Sample traces (L) and quantification of mEPSC frequencies (M) and amplitudes (N) (Ca$_V$2 control, n = 19/3; Ca$_V$2 cTKO, n = 19/3).

All data are mean ± SEM; **p < 0.01 and ***p < 0.001. Mann-Whitney rank sum tests were used for statistical analyses. For Ca$_V$2.2 conditional gene ablation and additional analyses, see Figure S1.

between the electron-dense vesicular and plasma membranes) were unaffected. Hence, Ca$_V$2 channels are not involved in the tethering or docking of synaptic vesicles.

Synaptic strength stems from the product of the number of vesicles in the readily releasable pool (RRP) and the release probability (p) of each vesicle. To better assess these parameters in Ca$_V$2 cTKO synapses, we measured RRP and evaluated presynaptic Ca^{2+} entry as a key determinant of p (Zucker and Regehr, 2002). Consistent with normal synapse numbers and ultrastructure, release measured as the EPSC during a 10 s application of hypertonic sucrose was unchanged (Figures 2E and 2F). This is often used as a measure of RRP, and release evoked by hypertonic sucrose may stem from identical or overlapping pools and may recruit vesicles that are not accessible to action potentials (Kaeser and Regehr, 2017). Single action potential-triggered Ca^{2+} entry into individual boutons (Held et al., 2016; Liu et al., 2014) was strongly impaired upon Ca$_V$2 cTKO (Figures 2G–2I and S2D). Although most Ca$_V$2 cTKO boutons had virtually no Ca^{2+} entry, a few exhibited sizeable transients ($\Delta F/F_0 > 1$; 18% in Ca$_V$2 cTKO, 92% in Ca$_V$2 control; Figure 2H). Blockers of Ca$_V$1, Ca$_V$2.1, and Ca$_V$2.2 did not remove this leftover Ca^{2+} entry, but blocking action potentials did (Figures S2D and S2E). Furthermore, single-knockout neurons for individual Ca$_V$2s are completely insensitive to the corresponding blockers

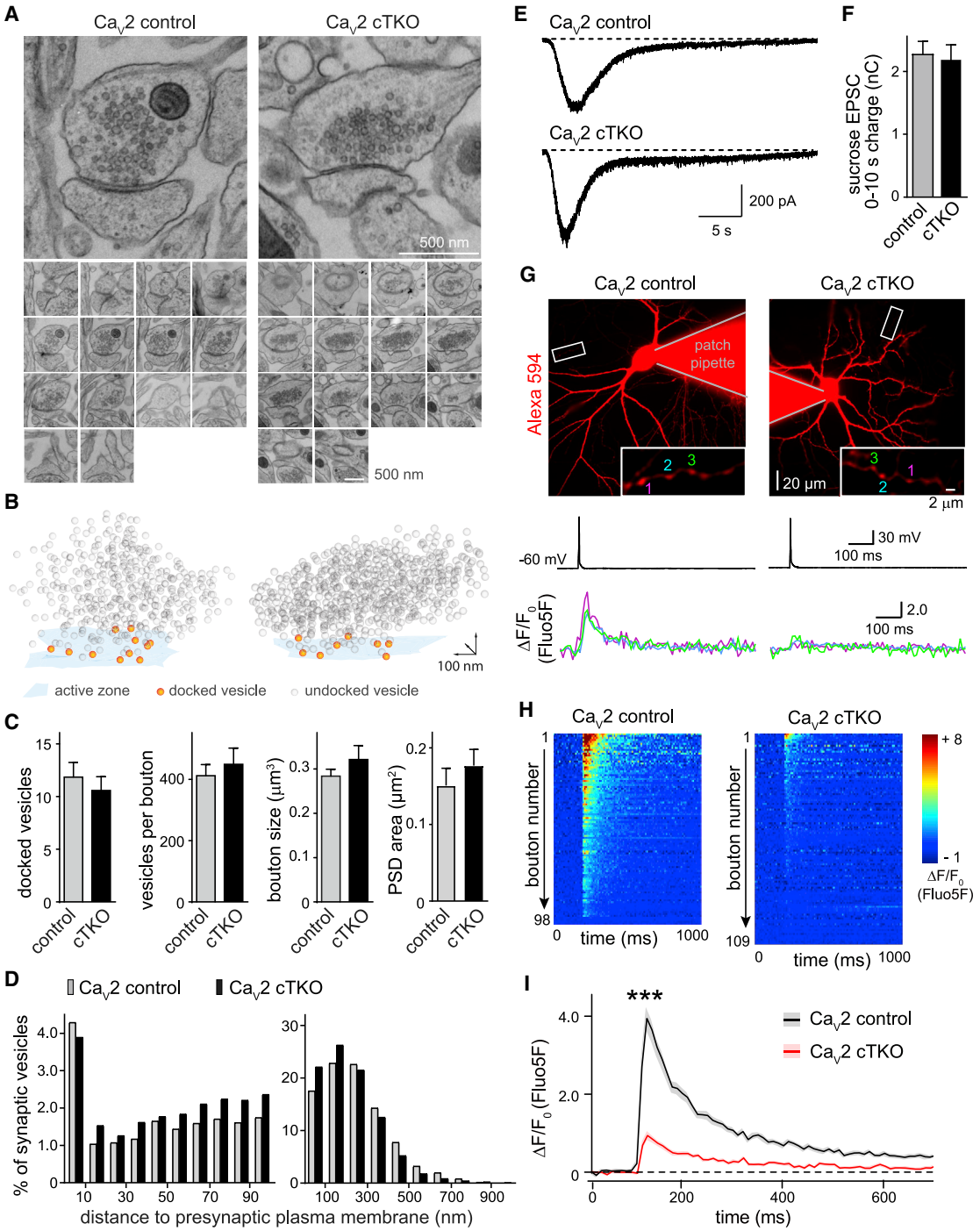

Figure 2. Strongly Impaired Ca^{2+} Entry but Normal Synaptic Ultrastructure in Ca_V2 cTKO

(A–D) Sample electron microscopic images (A), 3D reconstructions (B), and quantification (C and D) of serially sectioned synapses of high-pressure frozen neurons; all parameters in (C) are averages per synapse. Histograms in (D) show vesicle distributions in 10 nm (left) or 100 nm (right) bins (Ca_V2 control, n = 12 synapses/2 independent cultures; Ca_V2 cTKO, n = 13/2).

(E and F) Sample traces (E) and quantification (F) of EPSCs during the first 10 s of local 500 mOsm sucrose superfusion (Ca_V2 control, n = 19 cells/3 independent cultures; Ca_V2 cTKO, n = 19/3).

(legend continued on next page)

(Figures S1C–S1F). Hence, Ca_V2 channels are the main source of Ca^{2+} entry at these synapses, and the small amount of remaining Ca^{2+} entry is likely mediated by other voltage-gated channels. Removing Ca_V2 channels leads to a loss of Ca^{2+} entry and triggering of release, but synaptic vesicle tethering, docking, and priming are unaffected.

Active Zone Assembly Persists in the Absence of Ca_V2 Channels

To assess active zone protein complexes at synapses, we performed stimulated emission depletion (STED) microscopy, as we previously reported (de Jong et al., 2018; Wong et al., 2018). In brief, we identified side-view synapses by a bar-like postsynaptic density (PSD; marked by PSD-95, imaged using STED) that was aligned at one edge of a synaptic vesicle cloud (imaged by confocal microscopy) and assessed localization of a test protein (imaged using STED) relative to these markers (Figures S3A–S3D). In some cases, the active zone marker Bassoon (stained by antibodies against Bassoon N- and C-termini, named $Bassoon^N$ and $Bassoon^C$, respectively) was used instead of PSD-95 for side-view identification. PSD-95 was 92 ± 3 nm away from $Bassoon^C$, and $Bassoon^N$ signals were localized 68 ± 3 nm toward the inside of nerve terminals from $Bassoon^C$ (Figures 3A–3D).

We next assessed Ca_V2 control and cTKO synapses. Overall PSD-95 fluorescence was unaffected by Ca_V2 cTKO (Figures S3E–S3G). $Ca_V2.1$ and $Ca_V2.2$ were clustered as bars with peaks at 85 ± 3 and 77 ± 5 nm from PSD-95 peak fluorescence, respectively. Ca_V2 ablation removed the active zone peak, establishing signal specificity (Figures 3E, 3F, S3H, and S3I). We then analyzed antibody staining for RIM, RIM-BP2, Liprin-α3, ELKS2, Bassoon, and Munc13-1 and found that these proteins were clustered 70–100 nm away from the PSD-95 peak at Ca_V2 control and cTKO synapses (Figures 3G–3L and S3J–S3O). Similar results were obtained in neurons with very early cre infection (Figures S4A–S4L; transduced within 12 h after plating) or late cre infection (Figures S4M–S4R; infected at day *in vitro* [DIV] 10). Notably, there were small increases in ELKS2, Munc13-1, and Bassoon peak intensities. These changes could be compensatory in response to loss of activity or may reflect that binding sites of Ca^{2+} channel interacting proteins, for example of RIM, are more available to interact with other proteins, leading to enhanced active zone recruitment of these proteins. In summary, these experiments establish that active zone assembly was not disrupted upon Ca_V2 ablation.

Transsynaptic Protein Alignment in the Absence of Ca_V2 Channels

RIM and synaptic vesicle fusion are aligned with postsynaptic receptor and scaffold nanodomains (Tang et al., 2016), and Ca^{2+}-triggered exocytosis and Ca^{2+} channels are candidates for mediating this nanocolumnar organization (Biederer et al., 2017). We used 3D direct stochastic optical reconstruction microscopy (dSTORM) to test this hypothesis. We found that nanoscale lateral organization of RIM1 and PSD-95 was similar at Ca_V2 control and cTKO synapses (Figures 3M–3Q). Hence, consistent with the STED analyses, Ca_V2s do not control the nano-assemblies of RIM and PSD-95.

We next tested whether nanoclusters of PSD-95 and RIM remained aligned with one another. Cross-correlation analyses of RIM and PSD-95 localizations within individual synapses confirmed that their distributions were correlated with one another to a similar extent at Ca_V2 control and cTKO synapses (Figure 3R). Furthermore, in both genotypes, the presynaptic location of RIM nanoclusters predicted the postsynaptic distribution profile of PSD-95 (Figure 3S) and vice versa (Figure 3T). We conclude that neither the organization of protein within the face of the active zone nor the transsynaptic protein alignment in nanocolumns depends on Ca_V2s, Ca^{2+} entry through them, or exocytosis triggered by Ca_V2s.

Active Zone Assembly in the Absence of Voltage-Dependent Ca^{2+} Entry

To rule out that the small amount of Ca_V2-independent action potential-triggered Ca^{2+} entry (Figures 2G–2I) supported active zone or synapse assembly, we cultured control neurons and supplied the medium 12 h after plating with either the $Ca_V2.1$ and $Ca_V2.2$ blockers ω-Agatoxin IVA (ω-Aga; 200 nM) and ω-conotoxin GVIA (ω-Ctx; 250 nM) or with the same Ca_V2 blockers and the Na^+ channel blocker TTX (1 μM) to inhibit action potential firing. TTX eliminated stimulus-induced presynaptic Ca^{2+} entry (Figure S2D). Blockers were resupplied every 72 h for continuous, full suppression of voltage-dependent Ca^{2+} entry (see STAR Methods), and cultures were harvested at DIV 15 (Figure 4A).

Using STED microscopy, we found that active zones and postsynaptic densities were present and aligned with one another in side-view synapses despite the block of Ca^{2+} influx through $Ca_V2.1$ and $Ca_V2.2$. Similar to Ca_V2 cTKO, there were increases in the peak fluorescence of some active zone proteins upon Ca_V2 blockade. These increases were pronounced when action potentials were blocked on top of Ca^{2+} entry and accompanied by a significant elevation of PSD-95 (Figures 4B–4I and S5A–S5F), but were occluded in Ca_V2 cTKO neurons (Figures S5G and S5H). This supports the hypothesis that homeostatic adaptations lead to enhanced synaptic protein expression when activity is blocked throughout development either pharmacologically or by ablation of Ca_V2s.

Synaptic Transmission and Active Zone Assembly at Ca_V2 cTKO Calyces of Held

To assess whether Ca_V2s are dispensable for synapse assembly *in vivo*, we removed them at the calyx of Held synapse by injecting AAVs that co-express cre and cytosolic mCherry into the

(G–I) Sample images and traces (G) and quantification (H and I) of presynaptic Ca^{2+} transients. Neurons were filled with Alexa 594 (G, top, insets show axons) and Fluo5F through a patch pipette; the somatic action potential of the same neurons (middle), $\Delta F/F_0$ of three boutons (bottom, color codes as shown on top), plots of each bouton (H), and average $\Delta F/F_0$ (I) are shown (Ca_V2 control, n = 98 boutons/8 cells/4 independent cultures; Ca_V2 cTKO, n = 109/10/4).
Data are mean ± SEM; ***$p < 0.001$. Mann-Whitney rank sum tests were used for (C) and (F), and two-way ANOVA for (I, over the first 60 ms window following the action potential). For single-section electron microscopic analyses and pharmacological tests of Ca^{2+} transients, see Figure S2.

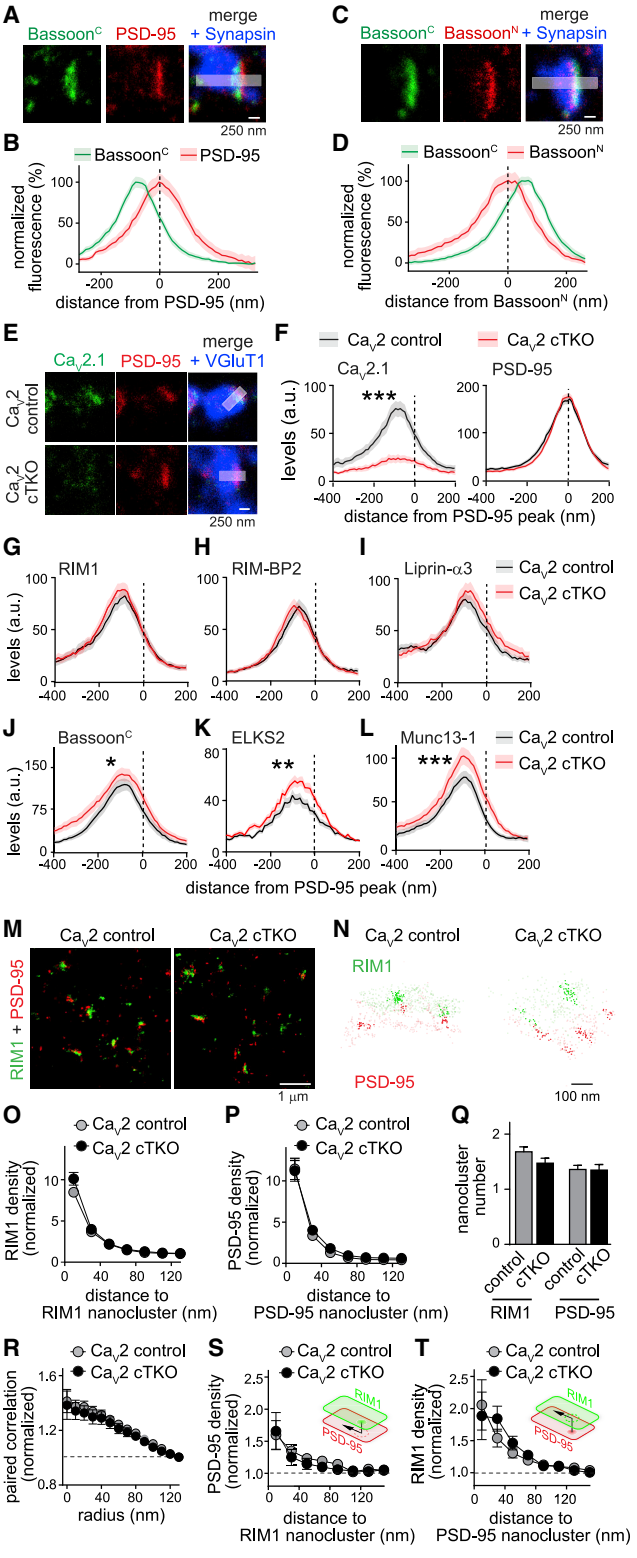

Figure 3. Intact Synaptic Nanostructure of Ca_V2 cTKO Synapses

(A–D) Sample STED images (A and C) and quantification (B and D) of wild-type side-view synapses stained for Bassoon C-termini (Bassoon^C, STED) and PSD-95 (STED) or Bassoon N-termini (Bassoon^N, STED) and Bassoon^C (STED), respectively, and the vesicle marker Synapsin (confocal). Intensity profiles (shaded area) quantified and aligned to the peaks of PSD-95 (B, dashed line; n = 38 synapses/3 independent cultures) or Bassoon^N (D, dashed line; n = 60/3).

(E and F) Sample images (E) and quantification (F) of synapses stained for $Ca_V2.1$ (STED), PSD-95 (STED), and VGluT1 (confocal). Intensity profiles (only the areas shown in F are shaded in E) were aligned to the PSD-95 peak (dashed line; Ca_V2 control, n = 61/3; Ca_V2 cTKO, n = 58/3).

(G–L) Intensity profiles of neurons stained for RIM1 (G; Ca_V2 control, n = 56/3; Ca_V2 cTKO, n = 55/3), RIM-BP2 (H; Ca_V2 control, n = 61/3; Ca_V2 cTKO, n = 60/3), Liprin-α3 (I; Ca_V2 control, n = 60/3; Ca_V2 cTKO, n = 55/3), Bassoon^C (J; Ca_V2 control, n = 38/3; Ca_V2 cTKO, n = 40/3), ELKS2 (K; Ca_V2 control, n = 59/3; Ca_V2 cTKO, n = 60/3), and Munc13-1 (L; Ca_V2 control, n = 59/3; Ca_V2 cTKO, n = 57/3).

(M and N) Sample dSTORM images (M) and localizations (N, with nanoclusters highlighted) of RIM1 and PSD-95 antibody stained neurons.

(O and P) Protein enrichment as a function of distance from protein nanocluster center for RIM1 (O; Ca_V2 control, n = 128 nanoclusters/74 synapses/3 independent cultures; Ca_V2 cTKO, n = 100/66/3) and PSD-95 (P; Ca_V2 control, n = 91/69/3; Ca_V2 cTKO, n = 85/61/3).

(Q) Nanocluster numbers per synapse for RIM1 and PSD-95 (Ca_V2 control, n = 81 synapses/3 independent cultures; Ca_V2 cTKO, n = 81/3).

(R) Paired cross-correlation ($g_c[r]$, y axis) of RIM1 and PSD-95 localizations (Ca_V2 control, n = 75 synapses/3 independent cultures; Ca_V2 cTKO, n = 71/3).

(S and T) PSD-95 enrichment as a function of distance from RIM1 nanocluster centers (S; Ca_V2 control, n = 106 nanoclusters/75 synapses/3 independent cultures; Ca_V2 cTKO, n = 84/59/3) or vice versa (T; Ca_V2 control, n = 101/68/3; Ca_V2 cTKO, n = 84/64/3).

All data are mean ± SEM; *p < 0.05, **p < 0.01, and ***p < 0.001. Statistical comparisons were performed using two-way ANOVA for (F) and (G)–(L). The Mann-Whitney rank-sum test was performed for (Q) and the Mann-Whitney rank-sum test with post hoc Holm-Sidak test to correct for multiple comparisons for (O), (P), and (R)–(T). For example images and PSD-95 analyses for (G)–(L), see Figure S3, and for analyses upon early (DIV 0) or late (DIV 10) cre infection, see Figure S4.

anterior ventral cochlear nucleus (AVCN) of newborn Ca_V2 triple floxed (to generate cTKO calyces) or wild-type (to generate control calyces) mice (Figures 5A and 5B). We then measured evoked EPSCs and examined presynaptic morphology at labeled calyces at postnatal days 13–16 (P13–P16). Evoked EPSCs were essentially absent at cTKO calyces (Figures 5C–5F), but no changes in synaptic vesicle proteins or the active zone proteins Bassoon, RIM, and ELKS2 (Figures 5G–5K and S5I–S5P) were detected. We conclude that, as in cultured neurons, active zone and synapse assembly at the calyx of Held do not necessitate Ca_V2s, Ca_V2-mediated Ca^{2+} entry, and synaptic vesicle exocytosis.

α2δ-1 Localizes to Nerve Terminals Independent of Ca_V2 Channels

β and α2δ proteins are associated with Ca_V2s and are necessary for $Ca_V2.1$-mediated currents in transfected HEK293T cells (Figures 6A–6C and S6C–S6K). Given this association, their localization may be disrupted in Ca_V2 cTKO synapses, suggesting that these proteins are also not controlling synapse structure. This hypothesis is contrasted by studies that found structural changes after manipulation of α2δs (Fell et al., 2016; Hoppa et al., 2012; Kerov et al., 2018; Pirone et al., 2014; Schneider et al., 2015; Wang et al., 2017). Alternatively, α2δ proteins could have roles independent of the presence of α1. To distinguish between these possibilities, we assessed whether the synaptic

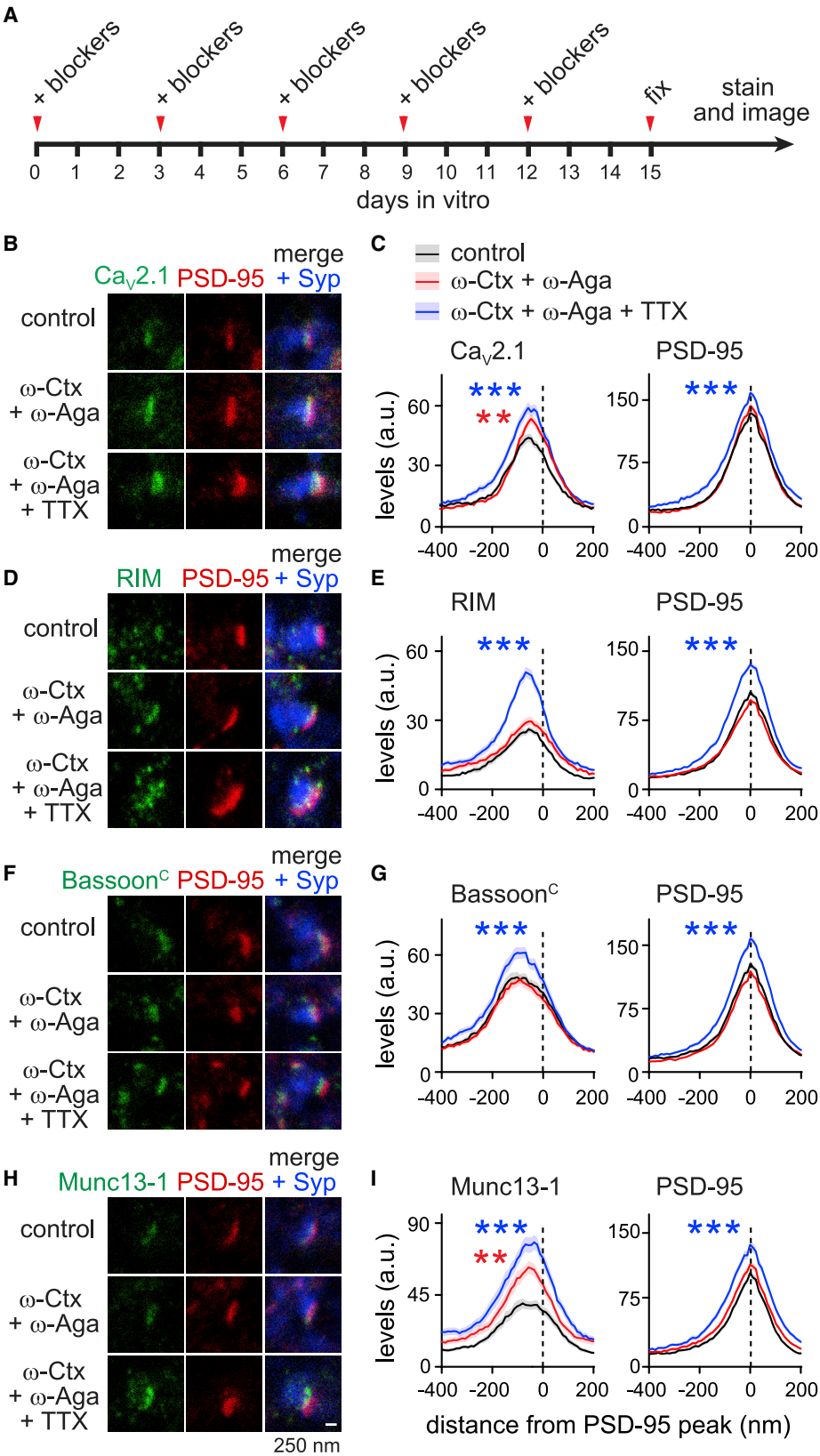

(legend on next page)

localization of β and α2δ proteins is dependent on the presence of Ca_V2s.

Using confocal microscopy, we found that intensities of β1, β3, and β4 staining were markedly reduced at Ca_V2 cTKO synapses, while β2 staining was unaffected (Figures S6A and S6B). The remaining signal could either be non-specific or be contributed by β subunits that are associated with other Ca_Vs. We then used STED microscopy to assess α2δ-1 localization at the active zone and simultaneously validated the antibodies in neurons from conditional α2δ-1-knockout mice (Park et al., 2016). We focused on α2δ-1 because it is highly expressed in the hippocampus and has been studied for its role in trafficking, targeting, and modulating hippocampal Ca_V2s (Ferron et al., 2018; Hoppa et al., 2012; Schneider et al., 2015). In control neurons, α2δ-1 had a modest peak at ~200 nm from PSD-95 in side-view synapses, and there was widespread staining throughout nerve terminals. Compellingly, in Ca_V2 cTKO synapses, the α2δ-1 staining was not altered (Figures 6D–6F and S6L), while it was significantly reduced at α2δ-1 cKO synapses (Figures 6G–6I and S6M). The remaining staining in α2δ-1 cKO neurons could be from other α2δ proteins or unspecific background. Because of antibody incompatibilities, we could not directly test α2δ-1 and $Ca_V2.1$ co-localization. Instead, we assessed their relative localization by plotting the knockout-subtracted side-view profiles and found that their distributions did not overlap well (Figure S6N). Hence, the presence of α2δ-1 at synapses does not depend on Ca_V2s, and the distribution of α2δ-1 is broader than that of $Ca_V2.1$. Reciprocally, knockout of α2δ-1 did not impair evoked EPSCs or the localization of $Ca_V2.1$ (Figures S6O–S6R).

We next assessed α2δ-1 trafficking in transfected HEK293T cells and found that α2δ-1 and $Ca_V2.1$ were co-localized in the periphery of transfected cells that were permeabilized and antibody stained (Figures 6J–6L). Labeling of the cell surface pool of α2δ-1 without permeabilization revealed that its surface localization did not require the presence of $Ca_V2.1$ (Figures 6M and 6N). We conclude that α2δ-1 localizes independently of Ca_V2 α1 to the cell surface and to nerve terminals. α2δ-1 may have roles in synapse structure, but these roles would be independent of the presence of Ca_V2s, similar to the fly neuromuscular junction (Kurshan et al., 2009).

Mechanisms of Ca_V2 Targeting to Active Zones

Thus far, all data strongly favor the anchored Ca_V2 model. To directly test this model and its underlying mechanisms, we rescued $Ca_V2.1$ expression in Ca_V2 cTKO neurons. We first expressed full-length, HA-tagged $Ca_V2.1$ α1 in Ca_V2 cTKO synapses using lentiviral expression. The tag was inserted in the intracellular N-terminus in a sequence that tolerates knockin of a fluorescent protein (Mark et al., 2011). In STED images, the rescue Ca^{2+} channel localized in a bar-like structure to active zones of synapses (Figures 7A-7D). The HA antibody signal peaked at 64 ± 11 nm from PSD-95 peak fluorescence, similar but slightly closer to PSD-95 than the $Ca_V2.1$ antibody signal, possibly because the $Ca_V2.1$ antibodies bind to the extended, flexible C-terminus (antigen K_{1921}-Q_{2212}), while the HA tag is inserted in the N-terminus closer to the plasma membrane. This rescue approach nearly completely restored IPSCs in Ca_V2 cTKO neurons, mediated EPSCs at levels above control (Figures 7E–7H), and did not influence the vesicle pool released by hypertonic sucrose (Figures S7A–S7D).

Previous studies indicated that protein interactions of the intracellular Ca_V2 C-terminus might be important for Ca_V2 active zone recruitment (Acuna et al., 2016; Hibino et al., 2002; Kaeser et al., 2011; Lübbert et al., 2017; Maximov and Bezprozvanny, 2002; Wang et al., 2016). We generated a truncated $Ca_V2.1$ version in which we removed the entire intracellular C-terminus (deletion of residues L_{1775}–C_{2368}, "$Ca_V2.1$-ΔCt"; Figures 7A, 7B, and S7E). $Ca_V2.1$-ΔCt was expressed efficiently in neurons and transfected HEK293T cells (Figures S7F–S7H). However, no active zone or synaptic localization could be detected (Figures 7C and 7D), but instead $Ca_V2.1$-ΔCt displayed increased somatic presence (Figures S7F and S7G). $Ca_V2.1$-ΔCt failed to rescue EPSCs or IPSCs (Figures 7E–7H) or to mediate currents in transfected HEK293T cells (Figures S7H and S7J). Although several potential mechanisms may contribute, this finding is consistent with roles of the C-terminus in Ca^{2+} channel trafficking to synapses and justifies detailed studies of the $Ca_V2.1$ C-terminus.

To directly test roles of specific protein interactions, we mutated three sites in the $Ca_V2.1$ C-terminus (Figures 7A and S7E): (1) We truncated the last four amino acids (residues $_{2365}$DDWC$_{2368}$, to generate $Ca_V2.1^{\Delta P}$), which are necessary for binding to the PDZ domain of the active zone protein RIM (Kaeser et al., 2011; Wu et al., 2019); (2) We mutated $_{2239}$PxxP$_{2242}$ to $_{2239}$AxxA$_{2242}$ (to generate $Ca_V2.1^{AxxA}$), which abolishes binding to RIM-BP (Hibino et al., 2002; Kaeser et al., 2011; Wu et al., 2019); (3) We removed amino acids S_{2016}–R_{2060} (to generate $Ca_V2.1^{\Delta K}$), a motif recently found to contribute to $Ca_V2.1$ active zone targeting (Lübbert et al., 2017) but without a known interaction partner. This motif contains a short polylysine stretch (hence "K") and a PxxP motif (Figure S7E).

We expressed single (Figures S8A–S8F), double (Figures S8G–S8L), or triple (Figures 8A–8G) mutant channels using lentiviruses in Ca_V2 cTKO neurons and assessed channel localization and synaptic transmission and tested the mutants in transfected HEK293T cells (Figures S9A–S9F). Active zone levels

Figure 4. Ca^{2+} Entry Is Not Required for Active Zone Assembly

(A) Schematic of the experiment. Ca_V2 blockers alone (200 nM ω-Aga and 250 nM ω-Ctx) or blockers with TTX (1 μM) were added every 72 h.

(B and C) Sample images (B) and quantification (C) of side-view synapses, stained for $Ca_V2.1$ (STED), PSD-95 (STED), and Synaptophysin (Syp; confocal). Intensity profiles are aligned to the PSD-95 peak (dashed line; control, n = 63 synapses/3 independent cultures; ω-Ctx + ω-Aga, n = 72/3; ω-Ctx + ω-Aga + TTX, n = 71/3).

(D–I) Similar to (B) and (C) but stained for RIM (D and E; control, n = 56/3; ω-Ctx + ω-Aga, n = 54/3; ω-Ctx + ω-Aga + TTX, n = 78/3), Bassoon^C (F and G; control, n = 73/3; ω-Ctx + ω-Aga, 75/3; ω-Ctx + ω-Aga + TTX, 79/3) and Munc13-1 (H and I; control, n = 73/3; ω-Ctx + ω-Aga, 75/3; ω-Ctx + ω-Aga + TTX, 67/3).

All data are mean ± SEM; $^{**}p < 0.01$ and $^{***}p < 0.001$. Statistical comparisons were performed using two-way ANOVA, and post hoc Tukey's test was performed to compare drug groups with control. For analyses of PSD-95 levels, see Figure S5.

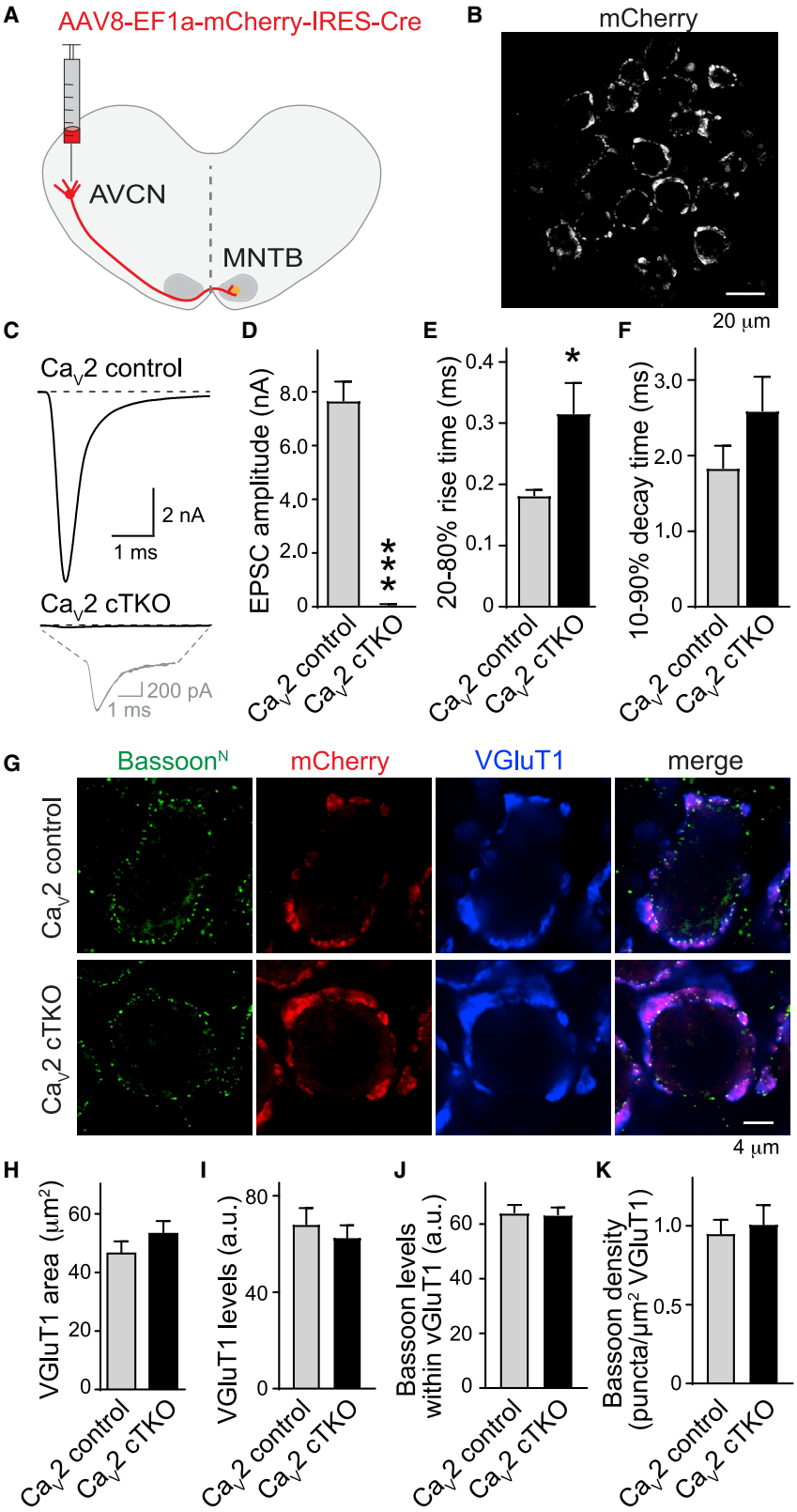

Figure 5. Synapse and Active Zone Assembly Persist after Ca$_V$2 cTKO at the Calyx of Held

(A and B) Schematic (A; AVCN, anterior ventral cochlear nucleus; MNTB, medial nucleus of the trapezoid body) and confocal image (B; MNTB) of the experiment. Adeno-associated viruses (AAVs) that co-express Cre and mCherry were injected at P1 into the AVCN in wild-type (to generate Ca$_V$2 control) or Ca$_V$2 triple floxed (to generate Ca$_V$2 cTKO) mice, and analyses were performed at P13–P16.

(C–F) Example traces (C, zoom-in in gray) and quantification (D–F) of AMPA-EPSCs measured in the MNTB principal cells and evoked by fiber stimulation (Ca$_V$2 control, n = 11 cells/3 mice; Ca$_V$2 cTKO, n = 8/3).

(G–K) Representative images (G) and quantification (H–K) of single-section confocal images stained for Bassoon^N and VGluT1 (Ca$_V$2 control, n = 14 calyces/3 mice; Ca$_V$2 cTKO, n = 16/3).

All data are mean ± SEM; *p < 0.05 and ***p < 0.001. The Mann-Whitney rank-sum test was performed for (D)–(F) and (H)–(K). For analyses of RIM and ELKS, see Figure S5.

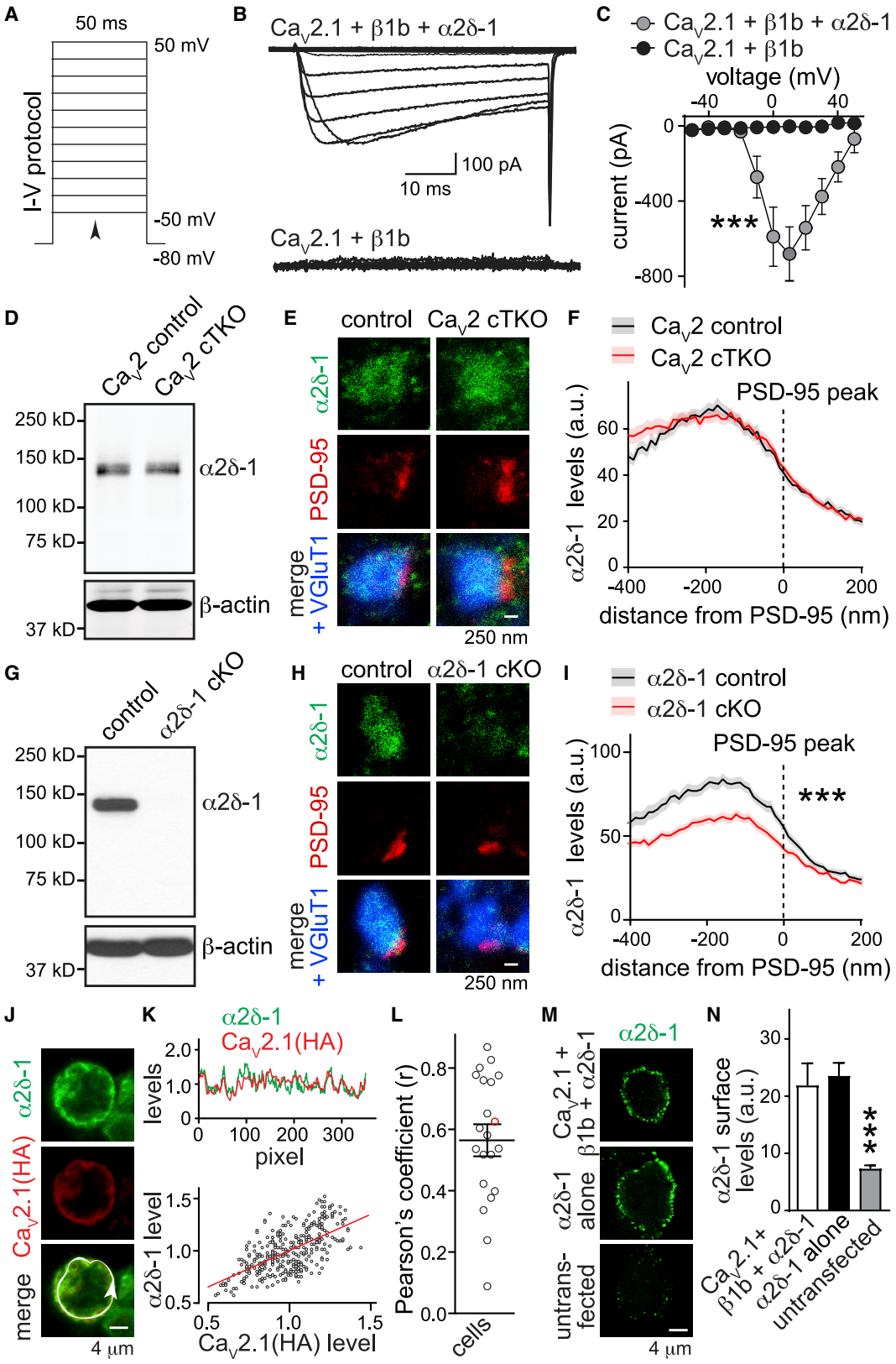

(legend on next page)

were mildly but significantly reduced in $Ca_V2.1^{\Delta P}$ and $Ca_V2.1$-^{AxxA}, while $Ca_V2.1^{\Delta K}$ did not measurably impair localization (Figures S8A–S8C). Simultaneously mutating two sites enhanced localization defects for most combinations (Figures S8G–S8I), and we observed a ~50% reduction in active zone peak localization but overall expression levels similar to the wild-type rescue channel when we mutated all three sites (Figures 8A–8C and S9G–S9I).

We next measured synaptic transmission in the same conditions (Figures 8D–8G, S8D–S8F, and S8J–S8L). Combinations of mutations impaired synaptic transmission more significantly than single-site mutations, with the triple mutant leading to a ~45% reduction in rescue efficacy compared with wild-type rescue channels (Figures 8D–8G). Electrophysiological recordings in transfected HEK293T cells further revealed that some mutations impaired $Ca_V2.1$ function (Figures S9A–S9F), with $Ca_V2.1^{\Delta K}$ leading to mild impairments in I/V relationship, activation, or inactivation when combined with $Ca_V2.1^{\Delta P}$ and/or $Ca_V2.1^{AxxA}$.

These experiments establish that redundant interactions of the $Ca_V2.1$ C-terminus control $Ca_V2.1$ localization, and they support the model in which RIM and RIM-BP are important channel anchoring proteins (Acuna et al., 2016; Heck et al., 2019; Hibino et al., 2002; Kaeser et al., 2011; Liu et al., 2011; Wu et al., 2019). Our results further indicate that additional targeting mechanisms must be present to account for the ~50% targeted channels when RIM and RIM-BP binding sites and the polylysine stretch are removed (Figure 8).

DISCUSSION

The analysis of central nervous synapses that lack Ca_V2 channels reveals five major findings (Figure 8H). First, synchronous release necessitates Ca_V2 channels, and Ca_V1 or Ca_V3 cannot compensate for the loss of Ca_V2s. Second, Ca_V2s and Ca^{2+} entry through them are dispensable for active zone assembly and for vesicle docking and priming. Third, α2δ-1, a protein that may have roles in synapse assembly, does not depend on the presence of Ca_V2s for its presynaptic localization. Fourth, the nano-alignment of release-site proteins with postsynaptic scaffold domains does not require Ca_V2 channels. Finally, Ca_V2 C-terminal sequences are essential for active zone delivery and anchoring of these channels.

Ca_V2 Channels and Ca^{2+} Entry through Them Do Not Control Synapse Nanostructure

Like many important synaptic proteins, Ca_V2 channels are expressed from families of paralogous genes in the vertebrate brain (Koopmans et al., 2019). This complexity precluded their study using complete Ca_V2 loss-of-function approaches, and multiple hypotheses and mechanisms have been presented for their roles in synapse structure. Here, we summarize these previous studies in two models. In the Ca_V2-driven assembly model, Ca_V2 channels are essential nucleators of synapses or release sites. Such roles could be mediated by a scaffolding function of the Ca_V2 protein or rely on Ca^{2+} entry through these channels followed by local Ca^{2+} signaling mechanisms. In the anchored Ca_V2 model, the apparatus for synaptic transmission is scaffolded independent of Ca_V2 channels, but this apparatus anchors channels to release sites. Our experiments strongly favor the anchored Ca_V2 model because active zones and synapses remain assembled *in vitro* and *in vivo* when Ca_V2 channels are absent or Ca^{2+} entry is blocked, and rescue experiments directly support the anchored Ca_V2 model.

Our data do not fully exclude mild structural alterations. It is possible that Ca_V2s have some assembly roles that are redundant with other proteins, and homeostatic adaptations, perhaps similar to those operating at other synapses (Davis and Müller, 2015), may attempt to compensate for the loss of Ca^{2+} channels, Ca^{2+} entry, and exocytosis. Such assembly roles may be apparent when channels are overexpressed or in *in vitro* studies, in which Ca_V2s mediate expansion of active zone protein assemblies (Lübbert et al., 2019; Wu et al., 2019), and they may explain EPSC rescue above control levels (Figure 7F). Nevertheless, Ca_V2s on their own have no major role in controlling synapse structure, including active zone assembly, vesicle docking, and transsynaptic nanocolumnar organization. Notably, recent studies proposed roles for Ca_V2s in vesicle docking. At the calyx of Held, docking was altered upon viral expression of a truncated $Ca_V2.1$ protein in $Ca_V2.1$ knockouts (Lübbert et al., 2017), and biochemical studies of interactions of Ca_V2 C-termini with vesicles support such roles

Figure 6. Presynaptic α2δ-1 Localization Is Independent of Ca_V2

(A–C) Voltage step protocol (A, arrowhead indicates approximate position of current measurement), sample traces (B), and quantification of the I-V relationship (C) of Ba^{2+} currents recorded from HEK293T cells transfected with $Ca_V2.1$ + β1b with or without α2δ-1 ($Ca_V2.1$ + β1b + α2δ-1, n = 23 cells/3 independent transfections; $Ca_V2.1$ + β1b, n = 16/3).

(D) Western blot of α2δ-1 in Ca_V2 control and Ca_V2 cTKO neurons.

(E and F) Sample STED images (E) and quantification (F) of intensity profiles of side-view synapses in Ca_V2 control and Ca_V2 cTKO neurons stained for α2δ-1 (STED), PSD-95 (STED), and VGluT1 (confocal; Ca_V2 control, n = 68 synapses/3 independent cultures; Ca_V2 cTKO, n = 61/3).

(G–I) The same experiment as in (D)–(F) but in α2δ-1 control and α2δ-1 cKO neurons (α2δ-1 control, n = 63/3; α2δ-1 cKO, n = 61/3).

(J–L) Sample image (J), quantification of that image (K), and summary (L) of co-localization of α2δ-1 and HA-tagged $Ca_V2.1$ in HEK293T cells transfected with $Ca_V2.1$ + β1b + α2δ-1. Correlation analyses (K; signals normalized in each channel) were performed for the intensities of each pixel along the edge of a transfected cells (J, arrowed circle), and Pearson's correlation coefficient (r) was calculated for each cell (individual circles in L, example cell from J and K shown in red; n = 21 cells/3 independent transfections).

(M and N) Sample images (M) and quantification (N) of surface staining of α2δ-1 in transfected HEK293T cells ($Ca_V2.1$ + β1b + α2δ-1, n = 9 images/3 transfections; α2δ-1 alone, n = 9/3; control, n = 9/3).

All data are mean ± SEM; ***p < 0.001. Statistical comparisons were performed using two-way ANOVA for (C), (F), and (I) or Kruskal-Wallis analysis of variance with post hoc Dunn's test comparing each condition with $Ca_V2.1$ + β1b + α2δ-1 for (L). For assessment of Ca_Vβ localization, comparison of $Ca_V2.1$ and α2δ-1 localization, and analyses of α2δ-1 cKO, see Figure S6.

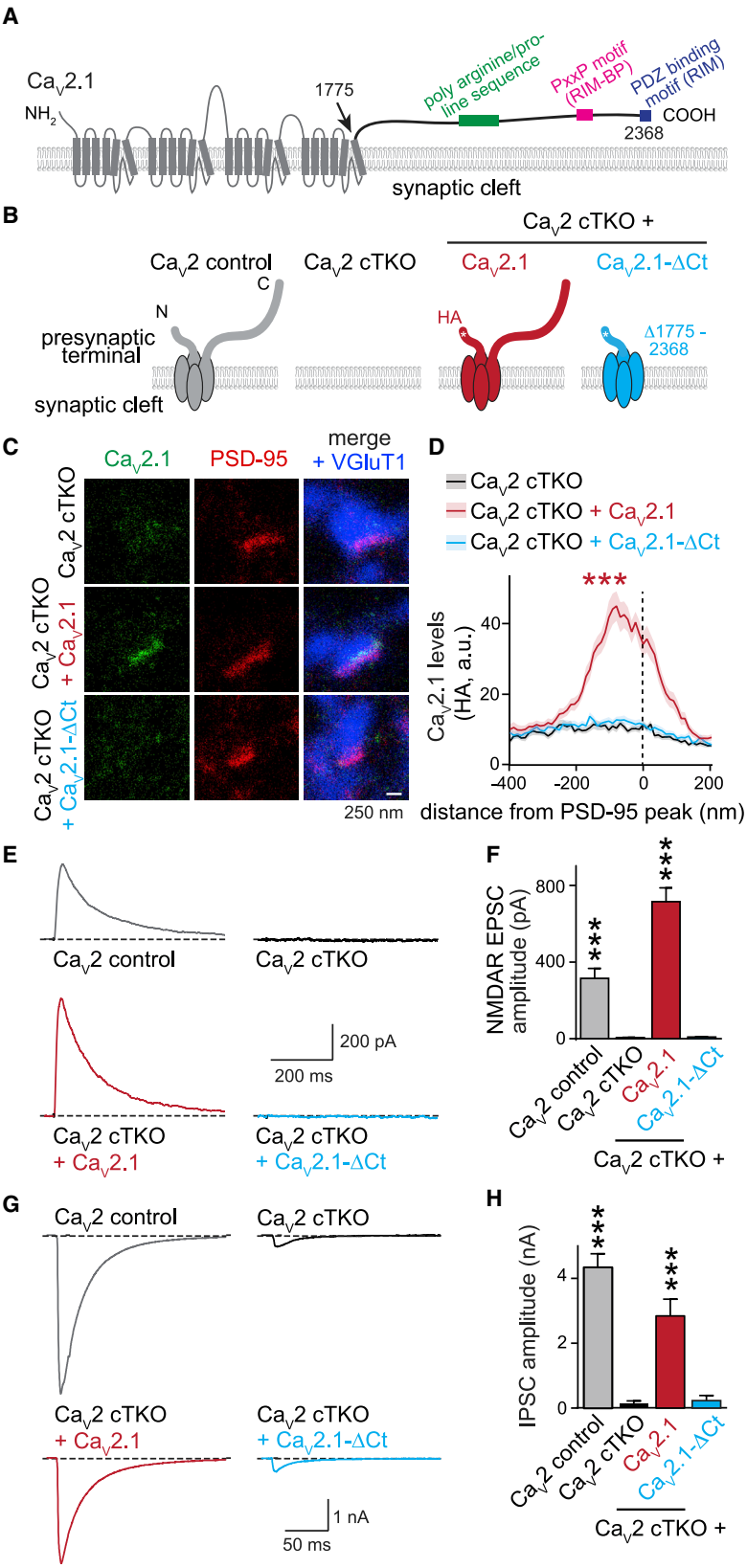

Figure 7. The Ca$_V$2.1 C-Terminus Is Essential for Ca^{2+} Channel Localization and Function

(A) Schematic of Ca$_V$2 α1 highlighting C-terminal interaction motifs.

(B) Schematic of rescue experiments of Ca$_V$2 cTKO neurons with HA-tagged (star) Ca$_V$2.1 or C-terminally truncated Ca$_V$2.1-ΔCt expressed by lentiviral transduction.

(C and D) Sample STED images (C) and quantification (D) of intensity profiles of side-view synapses of the experiment outlined in (B). Neurons were stained with antibodies for Ca$_V$2.1 (HA, STED), PSD-95 (STED), and VGluT1 (confocal; Ca$_V$2 cTKO, n = 59 synapses/3 cultures; Ca$_V$2 cTKO + Ca$_V$2.1, n = 57/3; Ca$_V$2 cTKO + Ca$_V$2.1-ΔCt, n = 60/3).

(E and F) Sample traces (E) and quantification (F) of NMDAR-EPSCs of the experiment outlined in (B) (Ca$_V$2 control, n = 18 cells/3 independent cultures; Ca$_V$2 cTKO, n = 18/3; Ca$_V$2 cTKO + Ca$_V$2.1, n = 18/3; Ca$_V$2 cTKO + Ca$_V$2.1-ΔCt, n = 18/3).

(G and H) As in (E) and (F), but for IPSCs (Ca$_V$2 control, n = 18/3; Ca$_V$2 cTKO, n = 15/3; Ca$_V$2 cTKO + Ca$_V$2.1, n = 17/3; Ca$_V$2 cTKO + Ca$_V$2.1-ΔCt, n = 16/3).

All data are mean ± SEM. ***p < 0.001. Data in (F) and (H) were analyzed using Kruskal-Wallis analysis of variance with post hoc Dunn's tests comparing each condition with Ca$_V$2 cTKO. Data in (D) were analyzed using two-way ANOVA, and post hoc Tukey's test was performed to compare rescue groups with Ca$_V$2 cTKO. For sequence alignments and analyses of readily releasable pool and somatic localization, see Figure S7.

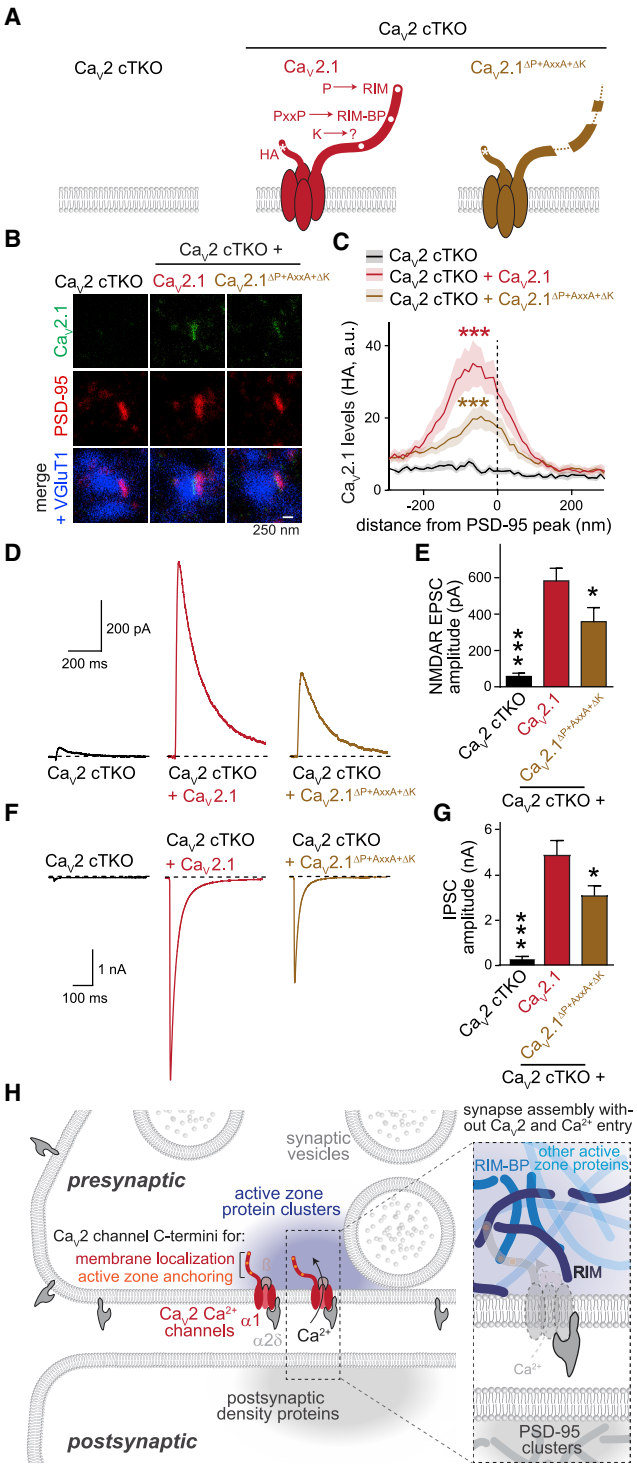

Figure 8. Multiple Interaction Sites in the Ca$_V$2.1 C-Terminus Mediate Ca$_V$2 Active Zone Localization

(A) Schematic of rescue experiments with HA-tagged Ca$_V$2 or triple mutant Ca$_V$2.1$^{\Delta P+AxxA+\Delta K}$. Tested interaction sites (white dots) and interaction partners are shown. Dashed lines indicate deletions or point mutations of specific sites.

(B and C) Sample STED images (B) and quantification (C) of intensity profiles of side-view synapses of the experiment outlined in (A), stained with antibodies for Ca$_V$2.1 (HA, STED), PSD-95 (STED), and VGluT1 (confocal). Dashed lines in (C) indicate the peak of PSD-95 (Ca$_V$2 cTKO, n = 40 synapses/3 independent cultures; Ca$_V$2 cTKO + Ca$_V$2.1, n = 53/3; Ca$_V$2 cTKO + Ca$_V$2.1$^{\Delta P+AxxA+\Delta K}$, n = 59/3).

(D and E) Sample traces (D) and quantification (E) of NMDAR-EPSCs of the experiment outlined in (A) (Ca$_V$2 cTKO, n = 14 cells/3 independent cultures; Ca$_V$2 cTKO + Ca$_V$2.1, n = 13/3; Ca$_V$2 cTKO + Ca$_V$2.1$^{\Delta P+AxxA+\Delta K}$, n = 12/3).

(F and G) As in (D) and (E) but for IPSCs (Ca$_V$2 cTKO, n = 18/3; Ca$_V$2 cTKO + Ca$_V$2.1, n = 19/3; Ca$_V$2 cTKO + Ca$_V$2.1$^{\Delta P+AxxA+\Delta K}$, n = 19/3).

(H) Model of the mechanisms of Ca$_V$2 channels in synapse assembly. Ca$_V$2 C-termini are important for synaptic and plasma membrane localization of the channels, and specific binding sites for RIM, RIM-BP, and other proteins redundantly mediate active zone anchoring. Synapse and active zone assembly, presynaptic localization of α2δ-1 proteins, and the nano-alignment of presynaptic and postsynaptic scaffolds are independent of Ca$_V$2s.

All data are mean ± SEM; *p < 0.05, **p < 0.01, and ***p < 0.001. Data in (C) were analyzed by two-way ANOVA, and statistical significance was assessed against Ca$_V$2.1 rescue using post hoc Tukey's test. Data in (E) and (G) were analyzed using Kruskal-Wallis analysis of variance with post hoc Dunn's tests comparing each condition to Ca$_V$2.1 rescue. See Figure S8 for single and double mutants and Figure S9 for assessment of Ba^{2+} currents and somatic levels.

(Gardezi et al., 2016; Snidal et al., 2018). Our experiments provide a direct test through assessing synapses without Ca$_V$2s, and argue strongly against roles in vesicle docking, at least at hippocampal synapses.

Another striking finding is that neither Ca$_V$2 channel proteins nor Ca^{2+} entry and exocytosis mediated by them are important for the nanocolumnar organization of active zone proteins and PSD-95 that aligns release sites with neurotransmitter receptors. This is surprising in light of experimental paradigms that change synaptic strength and lead to reorganization of nano-alignment (Hruska et al., 2018; Tang et al., 2016), as well as other aspects of synaptic nanostructure (Glebov et al., 2016; MacGillavry et al., 2013). How transsynaptic nano-alignment is established is unknown. One possibility is that nanostructure has an initial set point that is activity independent, but activity then regulates it after this setpoint is reached. Another possibility is that release that persists at Ca$_V$2 cTKO synapses, for example, miniature release, is sufficient to establish and maintain nano-alignment. Ultimately, our data are most consistent with a model in which transsynaptic nano-alignment reflects a developmental process and support the overall notion that synaptic vesicle exocytosis is dispensable for synapse structure at central nervous synapses (Sando et al., 2017; Sigler et al., 2017; Verhage et al., 2000). Because proteins that interact with Ca$_V$2s, including RIM, α2δ-1, and others, still localize normally at hippocampal synapses, our data do not exclude that these proteins are involved in transsynaptic organization independent of their association with Ca$_V$2s.

α2δ-1 Localizes Independent of the Presence of Ca$_V$2 Channels

Our experiments reveal that α2δ-1 is broadly distributed within nerve terminals, and there is at most partial co-localization of α2δ-1 and Ca$_V$2 at the level of STED microscopy. Subunits of a protein complex should associate with one another in the cellular compartment in which that complex executes its key functions, and the absence of the primary subunit of the complex should consequently lead to the absence of auxiliary subunits. In the

presented experiments, α2δ-1s do not possess these properties, and the data therefore suggest that they may not be stable subunits of Ca_V2 channels. This is consistent with previous biochemical assessment of Ca_V2 nano-environments and with single-particle tracking experiments, in which α2δ proteins only weakly associate with Ca_V2s (Müller et al., 2010; Voigt et al., 2016).

The results presented here indicate that roles of α2δ in hippocampal synapse structure may be independent of Ca_V2s and redundant among different α2δ proteins. Such roles may also be mediated by postsynaptic α2δ (Risher et al., 2018). The lack of dependence on Ca_V2 is similar to the fly neuromuscular junction, where presynaptic α2δ-3 controls synapse morphogenesis, but the α1 channel protein does not (Kurshan et al., 2009).

α2δ proteins robustly co-purify with Ca_V1 channels (Wu et al., 2016) but more weakly with Ca_V2 channels (Müller et al., 2010). This property, together with our results, may help explain a variety of observations. For instance, inner hair cell and retinal ribbon synapses rely on Ca_V1, and removal of either the pore-forming channel protein or of α2δs leads to presynaptic structural deficiencies (Kerov et al., 2018; Sheets et al., 2012; Wang et al., 2017). The possibility that ablation of Ca_V1 is accompanied by loss of α2δ, because of their stable association, could explain defects in synapse structure. A similar mechanism could be at play at vertebrate and *C. elegans* neuromuscular junctions, where Ca_V2s control aspects of synapse structure (Chen et al., 2011; Kushibiki et al., 2019; Nishimune et al., 2004; Tong et al., 2017). At hippocampal synapses, it is possible that α2δ proteins other than α2δ-1 associate with Ca_V2 channels, and future studies should systematically address the Ca_V2 subunit composition at various synapses. However, because knockout of Ca_V2 at hippocampal synapses does not induce structural deficits, these other subunits likely do not perform structural roles in association with Ca_V2 at the synapses we studied.

Mechanisms of the Ca_V2 C-Terminus

A body of work has shown that knocking out key active zone proteins leads to reduced levels of Ca_V2s or reduced presynaptic Ca^{2+} entry. This has been found for RIM (Han et al., 2011; Kaeser et al., 2011; Müller et al., 2012), RIM-BP (Liu et al., 2011), ELKS or its homolog Brp (Held et al., 2016; Kittel et al., 2006; Liu et al., 2014), as well as combinations of these knockouts (Acuna et al., 2016; Kushibiki et al., 2019; Wang et al., 2016). These findings have led to the anchored Ca_V2 model in which active zone proteins position Ca_V2s for rapid release. It was proposed that RIM, RIM-BP, and Ca_V2s form a tripartite complex that anchors Ca_V2s (Kaeser et al., 2011; Wu et al., 2019). Mutating relevant interaction sites on RIM led to a loss of ~50% of the channels at synapses (Kaeser et al., 2011), and mutating interaction sites in this tripartite complex also impaired the formation of liquid-phase condensates *in vitro* (Wu et al., 2019). We find that the Ca_V2 C-terminus is essential for targeting Ca_V2s to synapses and that mutating binding sites for RIM and RIM-BP resulted in ~50% reduced Ca_V2 levels at active zones. This reduction is qualitatively and quantitatively very similar to that in knockouts of active zone proteins and raises two important points.

First, some Ca_V2s are tethered to active zones independent of interactions with RIM and RIM-BP. An alternative complex that may tether Ca_V2s at synapses occurs with Mint and CASK (Maximov and Bezprozvanny, 2002). However, these proteins bind to similar regions on Ca_V2s (Maximov and Bezprozvanny, 2002; Maximov et al., 1999), and knockout of Mint or CASK does not lead to phenotypes indicative of an impairment in Ca_V2 targeting (Atasoy et al., 2007; Ho et al., 2006). Furthermore, C-terminal $Ca_V2.1$ splice variants that lack the interaction sites for these proteins can contribute to release when overexpressed (Heck et al., 2019). Hence, interactions other than those with Mint, CASK, RIM, and RIM-BP may be sufficient to target of some Ca_V2s.

Second, our data support key predictions of recent models in which phase separation mediates active zone assembly (Wu et al., 2019). In this model, low-affinity interactions account for targeting of Ca_V2s to active zones, and no single interaction is essential. Such redundancy was also observed in our rescue experiments, in which mutating multiple interaction sites was necessary to produce robust Ca_V2 targeting defects, but impairments remained partial. Similarly, deletion of active zone proteins resulted in an incomplete loss of Ca_V2s (Acuna et al., 2016; Kaeser et al., 2011; Liu et al., 2011; Müller et al., 2012; Wang et al., 2016). Ultimately, mechanisms for Ca_V2 targeting that rely on multiple dynamic and low-affinity interactions are well suited for regulation, and they may also account for variability in the properties of secretory sites across synapse types (Eggermann et al., 2011; Nakamura et al., 2015; Rebola et al., 2019). The work presented here lays the foundation for future studies addressing these questions.

STAR★METHODS

Detailed methods are provided in the online version of this paper and include the following:

- KEY RESOURCES TABLE
- RESOURCE AVAILABILITY
  - Lead Contact
  - Materials Availability
  - Data and Code Availability
- EXPERIMENTAL MODEL AND SUBJECT DETAILS
- METHOD DETAILS
  - Cell culture and lentiviral infection
  - Electrophysiological recordings from neurons
  - Electrophysiological recordings from HEK293T cells
  - Electrophysiological recordings at the calyx of Held
  - Presynaptic Ca^{2+} Imaging
  - Electron microscopy
  - Generation of custom antibodies
  - Western blotting
  - STED imaging
  - 3D STORM imaging
  - Confocal imaging in cultured neurons
  - Confocal imaging of calyces of Held in brain slices
  - Confocal imaging in transfected HEK293T cells
  - Statistics

SUPPLEMENTAL INFORMATION

Supplemental Information can be found online at https://doi.org/10.1016/j.neuron.2020.05.032.

ACKNOWLEDGMENTS

We thank J. Wang for technical support; Drs. W. Regehr, Bruce Bean, and A.-H. Tang and the Kaeser laboratory for comments and discussions; Drs. M. Verhage and J. Broeke for a MATLAB program to analyze electron microscopic images; and Drs. G. Feng and C. Dulla for providing α2δ-1 cKO mice. This work was supported by grants from the NIH (R01NS083898 and R01MH113349 to P.S.K., R01MH080046 to T.A.B., 5F31NS08907703 to R.G.H., and F31MH116583 to A.M.R.); the German Research Foundation (GRF Schn 387/21-1 to T.S.); the National Natural Science Foundation of China (31871033 to J.S.); the Harvard Brain Initiative (to P.S.K.); the Armenise Harvard Foundation (to P.S.K.); the Stuart H.Q. and Victoria Quan Fellowship (to R.G.H.); and the Alice and Joseph E. Brooks, the Fix, and the Gordon postdoctoral fellowships (to C.L.). We acknowledge the Neurobiology Imaging Facility (supported by P30 Core Center Grant NS072030) and the Electron Microscopy Facility at Harvard Medical School.

AUTHOR CONTRIBUTIONS

Conceptualization, R.G.H., C.L., and P.S.K.; Methodology, R.G.H., C.L., K.M., and J.W.; Formal Analysis, R.G.H., C.L., K.M., A.M.R., T.B.T., J.S., T.A.B., and P.S.K.; Investigation, R.G.H., C.L., K.M., A.M.R., T.B.T., G.D.N., S.S.H.W., and J.W.; Resources, A.M.J.M.v.d.M. and T.S.; Writing – Original Draft, R.G.H., C.L., and P.S.K.; Writing – Review & Editing, R.G.H., C.L., K.M., A.M.R., T.B.T., G.D.N., S.S.H.W., A.M.J.M.v.d.M., T.S., J.S., T.A.B., and P.S.K.; Supervision, J.S., T.A.B., and P.S.K.; Funding Acquisition, T.S., J.S., T.A.B., and P.S.K.

DECLARATION OF INTERESTS

The authors declare no competing interests. S.S.H.W. is currently an employee of RA Capital Management, LP.

Received: October 28, 2019
Revised: April 24, 2020
Accepted: May 21, 2020
Published: June 16, 2020

REFERENCES

Acuna, C., Liu, X., and Südhof, T.C. (2016). How to make an active zone: unexpected universal functional redundancy between RIMs and RIM-BPs. Neuron *91*, 792–807.

Atasoy, D., Schoch, S., Ho, A., Nadasy, K.A., Liu, X., Zhang, W., Mukherjee, K., Nosyreva, E.D., Fernandez-Chacon, R., Missler, M., et al. (2007). Deletion of CASK in mice is lethal and impairs synaptic function. Proc. Natl. Acad. Sci. U S A *104*, 2525–2530.

Biederer, T., Kaeser, P.S., and Blanpied, T.A. (2017). Transcellular nanoalignment of synaptic function. Neuron *96*, 680–696.

Bucurenciu, I., Kulik, A., Schwaller, B., Frotscher, M., and Jonas, P. (2008). Nanodomain coupling between Ca2+ channels and Ca2+ sensors promotes fast and efficient transmitter release at a cortical GABAergic synapse. Neuron *57*, 536–545.

Cantí, C., Nieto-Rostro, M., Foucault, I., Heblich, F., Wratten, J., Richards, M.W., Hendrich, J., Douglas, L., Page, K.M., Davies, A., and Dolphin, A.C. (2005). The metal-ion-dependent adhesion site in the Von Willebrand factor-A domain of alpha2delta subunits is key to trafficking voltage-gated Ca2+ channels. Proc. Natl. Acad. Sci. U S A *102*, 11230–11235.

Cao, Y.Q., Piedras-Rentería, E.S., Smith, G.B., Chen, G., Harata, N.C., and Tsien, R.W. (2004). Presynaptic Ca2+ channels compete for channel type-preferring slots in altered neurotransmission arising from Ca2+ channelopathy. Neuron *43*, 387–400.

Catterall, W.A. (2011). Voltage-gated calcium channels. Cold Spring Harb. Perspect. Biol. *3*, a003947.

Chen, J., Billings, S.E., and Nishimune, H. (2011). Calcium channels link the muscle-derived synapse organizer laminin β2 to Bassoon and CAST/Erc2 to organize presynaptic active zones. J. Neurosci. *31*, 512–525.

Chen, J.-H., Blanpied, T.A., and Tang, A.-H. (2020). Quantification of transsynaptic protein alignment: A data analysis case for single-molecule localization microscopy. Methods *174*, 72–80.

Davis, G.W., and Müller, M. (2015). Homeostatic control of presynaptic neurotransmitter release. Annu. Rev. Physiol. *77*, 251–270.

de Jong, A.P.H., Roggero, C.M., Ho, M.-R., Wong, M.Y., Brautigam, C.A., Rizo, J., and Kaeser, P.S. (2018). RIM C_2B domains target presynaptic active zone functions to PIP_2-containing membranes. Neuron *98*, 335–349.e7.

De Waard, M., Pragnell, M., and Campbell, K.P. (1994). Ca2+ channel regulation by a conserved beta subunit domain. Neuron *13*, 495–503.

Dietrich, D., Kirschstein, T., Kukley, M., Pereverzev, A., von der Brelie, C., Schneider, T., and Beck, H. (2003). Functional specialization of presynaptic Cav2.3 Ca2+ channels. Neuron *39*, 483–496.

Dymecki, S.M. (1996). Flp recombinase promotes site-specific DNA recombination in embryonic stem cells and transgenic mice. Proc. Natl. Acad. Sci. U S A *93*, 6191–6196.

Eggermann, E., Bucurenciu, I., Goswami, S.P., and Jonas, P. (2011). Nanodomain coupling between Ca^{2+} channels and sensors of exocytosis at fast mammalian synapses. Nat. Rev. Neurosci. *13*, 7–21.

Fell, B., Eckrich, S., Blum, K., Eckrich, T., Hecker, D., Obermair, G.J., Münkner, S., Flockerzi, V., Schick, B., and Engel, J. (2016). α2δ2 controls the function and trans-synaptic coupling of Cav1.3 channels in mouse inner hair cells and is essential for normal hearing. J. Neurosci. *36*, 11024–11036.

Fenno, L.E., Mattis, J., Ramakrishnan, C., Hyun, M., Lee, S.Y., He, M., Tucciarone, J., Selimbeyoglu, A., Berndt, A., Grosenick, L., et al. (2014). Targeting cells with single vectors using multiple-feature Boolean logic. Nat. Methods *11*, 763–772.

Ferron, L., Kadurin, I., and Dolphin, A.C. (2018). Proteolytic maturation of $\alpha_2\delta$ controls the probability of synaptic vesicular release. eLife *7*, e37507.

Gardezi, S.R., Nath, A.R., Li, Q., and Stanley, E.F. (2016). Characterization of a synaptic vesicle binding motif on the distal CaV2.2 channel C-terminal. Front. Cell. Neurosci. *10*, 145.

Glebov, O.O., Cox, S., Humphreys, L., and Burrone, J. (2016). Neuronal activity controls transsynaptic geometry. Sci. Rep. *6*, 22703.

Han, Y., Kaeser, P.S., Südhof, T.C., and Schneggenburger, R. (2011). RIM determines Ca^{2+} channel density and vesicle docking at the presynaptic active zone. Neuron *69*, 304–316.

Heck, J., Parutto, P., Ciuraszkiewicz, A., Bikbaev, A., Freund, R., Mitlöhner, J., Andres-Alonso, M., Fejtova, A., Holcman, D., and Heine, M. (2019). Transient confinement of $Ca_V2.1$ Ca^{2+}-channel splice variants shapes synaptic short-term plasticity. Neuron *103*, 66–79.e12.

Held, R.G., Liu, C., and Kaeser, P.S. (2016). ELKS controls the pool of readily releasable vesicles at excitatory synapses through its N-terminal coiled-coil domains. eLife *5*, e14862.

Hibino, H., Pironkova, R., Onwumere, O., Vologodskaia, M., Hudspeth, A.J., and Lesage, F. (2002). RIM binding proteins (RBPs) couple Rab3-interacting molecules (RIMs) to voltage-gated Ca(2+) channels. Neuron *34*, 411–423.

Ho, A., Morishita, W., Atasoy, D., Liu, X., Tabuchi, K., Hammer, R.E., Malenka, R.C., and Südhof, T.C. (2006). Genetic analysis of Mint/X11 proteins: essential presynaptic functions of a neuronal adaptor protein family. J. Neurosci. *26*, 13089–13101.

Hoppa, M.B., Lana, B., Margas, W., Dolphin, A.C., and Ryan, T.A. (2012). α2δ expression sets presynaptic calcium channel abundance and release probability. Nature *486*, 122–125.

Hruska, M., Henderson, N., Le Marchand, S.J., Jafri, H., and Dalva, M.B. (2018). Synaptic nanomodules underlie the organization and plasticity of spine synapses. Nat. Neurosci. *21*, 671–682.

Kaeser, P.S., and Regehr, W.G. (2014). Molecular mechanisms for synchronous, asynchronous, and spontaneous neurotransmitter release. Annu. Rev. Physiol. *76*, 333–363.

Kaeser, P.S., and Regehr, W.G. (2017). The readily releasable pool of synaptic vesicles. Curr. Opin. Neurobiol. *43*, 63–70.

Kaeser, P.S., Deng, L., Wang, Y., Dulubova, I., Liu, X., Rizo, J., and Südhof, T.C. (2011). RIM proteins tether Ca2+ channels to presynaptic active zones via a direct PDZ-domain interaction. Cell *144*, 282–295.

Kaeser, P.S., Deng, L., Fan, M., and Südhof, T.C. (2012). RIM genes differentially contribute to organizing presynaptic release sites. Proc. Natl. Acad. Sci. U S A *109*, 11830–11835.

Kerov, V., Laird, J.G., Joiner, M.L., Knecht, S., Soh, D., Hagen, J., Gardner, S.H., Gutierrez, W., Yoshimatsu, T., Bhattarai, S., et al. (2018). $\alpha_2\delta$-4 is required for the molecular and structural organization of rod and cone photoreceptor synapses. J. Neurosci. *38*, 6145–6160.

Kittel, R.J., Wichmann, C., Rasse, T.M., Fouquet, W., Schmidt, M., Schmid, A., Wagh, D.A., Pawlu, C., Kellner, R.R., Willig, K.I., et al. (2006). Bruchpilot promotes active zone assembly, Ca2+ channel clustering, and vesicle release. Science *312*, 1051–1054.

Kiyonaka, S., Wakamori, M., Miki, T., Uriu, Y., Nonaka, M., Bito, H., Beedle, A.M., Mori, E., Hara, Y., De Waard, M., et al. (2007). RIM1 confers sustained activity and neurotransmitter vesicle anchoring to presynaptic Ca2+ channels. Nat. Neurosci. *10*, 691–701.

Kiyonaka, S., Nakajima, H., Takada, Y., Hida, Y., Yoshioka, T., Hagiwara, A., Kitajima, I., Mori, Y., and Ohtsuka, T. (2012). Physical and functional interaction of the active zone protein CAST/ERC2 and the β-subunit of the voltage-dependent Ca(2+) channel. J. Biochem. *152*, 149–159.

Koopmans, F., van Nierop, P., Andres-Alonso, M., Byrnes, A., Cijsouw, T., Coba, M.P., Cornelisse, L.N., Farrell, R.J., Goldschmidt, H.L., Howrigan, D.P., et al. (2019). SynGO: an evidence-based, expert-curated knowledge base for the synapse. Neuron *103*, 217–234.e4.

Kurshan, P.T., Oztan, A., and Schwarz, T.L. (2009). Presynaptic alpha2delta-3 is required for synaptic morphogenesis independent of its Ca2+-channel functions. Nat. Neurosci. *12*, 1415–1423.

Kushibiki, Y., Suzuki, T., Jin, Y., and Taru, H. (2019). RIMB-1/RIM-binding protein and UNC-10/RIM redundantly regulate presynaptic localization of the voltage-gated calcium channel in *Caenorhabditis elegans*. J. Neurosci. *39*, 8617–8631.

Lin, Y., McDonough, S.I., and Lipscombe, D. (2004). Alternative splicing in the voltage-sensing region of N-type $Ca_V2.2$ channels modulates channel kinetics. J. Neurophysiol. *92*, 2820–2830.

Liu, K.S.Y., Siebert, M., Mertel, S., Knoche, E., Wegener, S., Wichmann, C., Matkovic, T., Muhammad, K., Depner, H., Mettke, C., et al. (2011). RIM-binding protein, a central part of the active zone, is essential for neurotransmitter release. Science *334*, 1565–1569.

Liu, C., Bickford, L.S., Held, R.G., Nyitrai, H., Südhof, T.C., and Kaeser, P.S. (2014). The active zone protein family ELKS supports Ca2+ influx at nerve terminals of inhibitory hippocampal neurons. J. Neurosci. *34*, 12289–12303.

Lübbert, M., Goral, R.O., Satterfield, R., Putzke, T., van den Maagdenberg, A.M., Kamasawa, N., and Young, S.M., Jr. (2017). A novel region in the $Ca_V2.1$ α_1 subunit C-terminus regulates fast synaptic vesicle fusion and vesicle docking at the mammalian presynaptic active zone. eLife *6*, e28412.

Lübbert, M., Goral, R.O., Keine, C., Thomas, C., Guerrero-Given, D., Putzke, T., Satterfield, R., Kamasawa, N., and Young, S.M., Jr. (2019). $Ca_V2.1$ α_1 subunit expression regulates presynaptic $Ca_V2.1$ abundance and synaptic strength at a central synapse. Neuron *101*, 260–273.e6.

Luebke, J.I., Dunlap, K., and Turner, T.J. (1993). Multiple calcium channel types control glutamatergic synaptic transmission in the hippocampus. Neuron *11*, 895–902.

MacGillavry, H.D., Song, Y., Raghavachari, S., and Blanpied, T.A. (2013). Nanoscale scaffolding domains within the postsynaptic density concentrate synaptic AMPA receptors. Neuron *78*, 615–622.

Mark, M.D., Maejima, T., Kuckelsberg, D., Yoo, J.W., Hyde, R.A., Shah, V., Gutierrez, D., Moreno, R.L., Kruse, W., Noebels, J.L., and Herlitze, S. (2011). Delayed postnatal loss of P/Q-type calcium channels recapitulates the absence epilepsy, dyskinesia, and ataxia phenotypes of genomic Cacna1a mutations. J. Neurosci. *31*, 4311–4326.

Maximov, A., and Bezprozvanny, I. (2002). Synaptic targeting of N-type calcium channels in hippocampal neurons. J. Neurosci. *22*, 6939–6952.

Maximov, A., Südhof, T.C., and Bezprozvanny, I. (1999). Association of neuronal calcium channels with modular adaptor proteins. J. Biol. Chem. *274*, 24453–24456.

Müller, C.S., Haupt, A., Bildl, W., Schindler, J., Knaus, H.G., Meissner, M., Rammner, B., Striessnig, J., Flockerzi, V., Fakler, B., and Schulte, U. (2010). Quantitative proteomics of the Cav2 channel nano-environments in the mammalian brain. Proc. Natl. Acad. Sci. U S A *107*, 14950–14957.

Müller, M., Liu, K.S.Y., Sigrist, S.J., and Davis, G.W. (2012). RIM controls homeostatic plasticity through modulation of the readily-releasable vesicle pool. J. Neurosci. *32*, 16574–16585.

Myoga, M.H., and Regehr, W.G. (2011). Calcium microdomains near R-type calcium channels control the induction of presynaptic long-term potentiation at parallel fiber to purkinje cell synapses. J. Neurosci. *31*, 5235–5243.

Nakamura, Y., Harada, H., Kamasawa, N., Matsui, K., Rothman, J.S., Shigemoto, R., Silver, R.A., DiGregorio, D.A., and Takahashi, T. (2015). Nanoscale distribution of presynaptic Ca(2+) channels and its impact on vesicular release during development. Neuron *85*, 145–158.

Nishimune, H., Sanes, J.R., and Carlson, S.S. (2004). A synaptic laminin-calcium channel interaction organizes active zones in motor nerve terminals. Nature *432*, 580–587.

Page, K.M., Rothwell, S.W., and Dolphin, A.C. (2016). The CaVβ subunit protects the I-II loop of the voltage-gated calcium channel $Ca_V2.2$ from proteasomal degradation but not oligoubiquitination. J. Biol. Chem. *291*, 20402–20416.

Park, J., Yu, Y.P., Zhou, C.-Y., Li, K.-W., Wang, D., Chang, E., Kim, D.-S., Vo, B., Zhang, X., Gong, N., et al. (2016). Central mechanisms mediating thrombospondin-4-induced pain states. J. Biol. Chem. *291*, 13335–13348.

Pereverzev, A., Mikhna, M., Vajna, R., Gissel, C., Henry, M., Weiergräber, M., Hescheler, J., Smyth, N., and Schneider, T. (2002). Disturbances in glucose-tolerance, insulin-release, and stress-induced hyperglycemia upon disruption of the Ca(v)2.3 (α1E) subunit of voltage-gated Ca(2+) channels. Mol. Endocrinol. *16*, 884–895.

Pirone, A., Kurt, S., Zuccotti, A., Rüttiger, L., Pilz, P., Brown, D.H., Franz, C., Schweizer, M., Rust, M.B., Rübsamen, R., et al. (2014). α2δ3 is essential for normal structure and function of auditory nerve synapses and is a novel candidate for auditory processing disorders. J. Neurosci. *34*, 434–445.

Rebola, N., Reva, M., Kirizs, T., Szoboszlay, M., Lőrincz, A., Moneron, G., Nusser, Z., and DiGregorio, D.A. (2019). Distinct nanoscale calcium channel and synaptic vesicle topographies contribute to the diversity of synaptic function. Neuron *104*, 693–710.e9.

Risher, W.C., Kim, N., Koh, S., Choi, J.-E., Mitev, P., Spence, E.F., Pilaz, L.-J., Wang, D., Feng, G., Silver, D.L., et al. (2018). Thrombospondin receptor α2δ-1 promotes synaptogenesis and spinogenesis via postsynaptic Rac1. J. Cell Biol. *217*, 3747–3765.

Sando, R., Bushong, E., Zhu, Y., Huang, M., Considine, C., Phan, S., Ju, S., Uytiepo, M., Ellisman, M., and Maximov, A. (2017). Assembly of excitatory synapses in the absence of glutamatergic neurotransmission. Neuron *94*, 312–321.e3.

Schindelin, J., Arganda-Carreras, I., Frise, E., Kaynig, V., Longair, M., Pietzsch, T., Preibisch, S., Rueden, C., Saalfeld, S., Schmid, B., et al. (2012). Fiji: an open-source platform for biological-image analysis. Nat. Methods *9*, 676–682.

Schneider, R., Hosy, E., Kohl, J., Klueva, J., Choquet, D., Thomas, U., Voigt, A., and Heine, M. (2015). Mobility of calcium channels in the presynaptic membrane. Neuron *86*, 672–679.

Schoch, S., Castillo, P.E., Jo, T., Mukherjee, K., Geppert, M., Wang, Y., Schmitz, F., Malenka, R.C., and Südhof, T.C. (2002). RIM1alpha forms a

protein scaffold for regulating neurotransmitter release at the active zone. Nature *415*, 321–326.

Scholz, K.P., and Miller, R.J. (1995). Developmental changes in presynaptic calcium channels coupled to glutamate release in cultured rat hippocampal neurons. J. Neurosci. *15*, 4612–4617.

Sheets, L., Kindt, K.S., and Nicolson, T. (2012). Presynaptic $Ca_V1.3$ channels regulate synaptic ribbon size and are required for synaptic maintenance in sensory hair cells. J. Neurosci. *32*, 17273–17286.

Sigler, A., Oh, W.C., Imig, C., Altas, B., Kawabe, H., Cooper, B.H., Kwon, H.-B., Rhee, J.-S., and Brose, N. (2017). Formation and maintenance of functional spines in the absence of presynaptic glutamate release. Neuron *94*, 304–311.e4.

Simms, B.A., and Zamponi, G.W. (2014). Neuronal voltage-gated calcium channels: structure, function, and dysfunction. Neuron *82*, 24–45.

Snidal, C.A., Li, Q., Elliott, B.B., Mah, H.K.-H., Chen, R.H.C., Gardezi, S.R., and Stanley, E.F. (2018). Molecular characterization of an SV capture site in the mid-region of the presynaptic $Ca_V2.1$ calcium channel C-terminal. Front. Cell. Neurosci. *12*, 127.

Südhof, T.C. (2012). The presynaptic active zone. Neuron *75*, 11–25.

Takahashi, T., and Momiyama, A. (1993). Different types of calcium channels mediate central synaptic transmission. Nature *366*, 156–158.

Tang, A.-H., Chen, H., Li, T.P., Metzbower, S.R., MacGillavry, H.D., and Blanpied, T.A. (2016). A trans-synaptic nanocolumn aligns neurotransmitter release to receptors. Nature *536*, 210–214.

Todorov, B., van de Ven, R.C.G., Kaja, S., Broos, L.A.M., Verbeek, S.J., Plomp, J.J., Ferrari, M.D., Frants, R.R., and van den Maagdenberg, A.M.J.M. (2006). Conditional inactivation of the Cacna1a gene in transgenic mice. Genesis *44*, 589–594.

Tong, X.-J., López-Soto, E.J., Li, L., Liu, H., Nedelcu, D., Lipscombe, D., Hu, Z., and Kaplan, J.M. (2017). Retrograde synaptic inhibition is mediated by α-neurexin binding to the $\alpha2\delta$ subunits of N-type calcium channels. Neuron *95*, 326–340.e5.

Verhage, M., Maia, A.S., Plomp, J.J., Brussaard, A.B., Heeroma, J.H., Vermeer, H., Toonen, R.F., Hammer, R.E., van den Berg, T.K., Missler, M., et al. (2000). Synaptic assembly of the brain in the absence of neurotransmitter secretion. Science *287*, 864–869.

Voigt, A., Freund, R., Heck, J., Missler, M., Obermair, G.J., Thomas, U., and Heine, M. (2016). Dynamic association of calcium channel subunits at the cellular membrane. Neurophotonics *3*, 041809.

Wang, S.S.H., Held, R.G., Wong, M.Y., Liu, C., Karakhanyan, A., and Kaeser, P.S. (2016). Fusion competent synaptic vesicles persist upon active zone disruption and loss of vesicle docking. Neuron *91*, 777–791.

Wang, Y., Fehlhaber, K.E., Sarria, I., Cao, Y., Ingram, N.T., Guerrero-Given, D., Throesch, B., Baldwin, K., Kamasawa, N., Ohtsuka, T., et al. (2017). The auxiliary calcium channel subunit $\alpha2\delta4$ is required for axonal elaboration, synaptic transmission, and wiring of rod photoreceptors. Neuron *93*, 1359–1374.e6.

Witcher, D.R., De Waard, M., Sakamoto, J., Franzini-Armstrong, C., Pragnell, M., Kahl, S.D., and Campbell, K.P. (1993). Subunit identification and reconstitution of the N-type Ca2+ channel complex purified from brain. Science *261*, 486–489.

Witcher, D.R., De Waard, M., Liu, H., Pragnell, M., and Campbell, K.P. (1995). Association of native Ca2+ channel beta subunits with the alpha 1 subunit interaction domain. J. Biol. Chem. *270*, 18088–18093.

Wong, M.Y., Liu, C., Wang, S.S.H., Roquas, A.C.F., Fowler, S.C., and Kaeser, P.S. (2018). Liprin-α3 controls vesicle docking and exocytosis at the active zone of hippocampal synapses. Proc. Natl. Acad. Sci. U S A *115*, 2234–2239.

Wu, L.-G., Borst, J.G.G., and Sakmann, B. (1998). R-type Ca2+ currents evoke transmitter release at a rat central synapse. Proc. Natl. Acad. Sci. U S A *95*, 4720–4725.

Wu, J., Yan, Z., Li, Z., Qian, X., Lu, S., Dong, M., Zhou, Q., and Yan, N. (2016). Structure of the voltage-gated calcium channel Ca(v)1.1 at 3.6 Å resolution. Nature *537*, 191–196.

Wu, X., Cai, Q., Shen, Z., Chen, X., Zeng, M., Du, S., and Zhang, M. (2019). RIM and RIM-BP form presynaptic active-zone-like condensates via phase separation. Mol. Cell *73*, 971–984.e5.

Zucker, R.S., and Regehr, W.G. (2002). Short-term synaptic plasticity. Annu. Rev. Physiol. *64*, 355–405.

STAR★METHODS

KEY RESOURCES TABLE

REAGENT or RESOURCE	SOURCE	IDENTIFIER
Antibodies		
rabbit anti-$Ca_V2.1$ (A46)	Synaptic Systems	Cat#: 152 203; RRID: AB_2619841
rabbit anti-$Ca_V2.2$ (1089, A37)	this study	N/A
mouse anti-$Ca_V\beta1$ (A86)	UC Davis/NIH Neuromab	Cat#:N7/18; RRID: AB_2750809
mouse anti-$Ca_V\beta2$ (A132)	UC Davis/NIH Neuromab	Cat#:N8B/1; RRID: AB_2750822
rabbit anti-$Ca_V\beta3$ (A20)	Alomone Labs	Cat#:ACC-008; RRID: AB_2039787
mouse anti-$Ca_V\beta4$ (A123)	UC Davis/NIH Neuromab	Cat#:73-054; RRID: AB_10671176
mouse anti-$\alpha2\delta$-1 (A174)	Sigma-Aldrich	Cat#: D219; RRID:AB_1078663
rabbit anti-$\alpha2\delta$-1 (A133)	Alomone Labs	Cat#:ACC-015; RRID: AB_2039785
rabbit anti-RIM1 (A58)	Synaptic Systems	Cat#: 140 003; RRID: AB_887774
rabbit anti-RIMBP2 (A126)	Synaptic Systems	Cat#: 316 103; RRID: AB_2619739
mouse anti-Bassoon N-terminal (A85)	Enzo Life Sciences	Cat#: ADI-VAM-PS003-F; RRID: AB_11181058
guinea pig anti-Bassoon C-terminal (A67)	Synaptic Systems	Cat#: 141 004; RRID: AB_2290619
rabbit anti-Liprin-$\alpha3$ (4396, A35)	Schoch et al., 2002, gift from Dr. T.C. Südhof	N/A
rabbit anti-ELKS2 (1029, A136)	Held et al., 2016	E3-1029
rabbit anti-Munc13-1 (A72)	Synaptic Systems	Cat#:126 103; RRID: AB_887733
mouse anti-PSD-95 (A149)	UC Davis/NIH Neuromab	Cat#: 73-028; RRID: AB_10698024
mouse anti-PSD-95	UC Davis/NIH Neuromab	Cat#: 75-028; RRID: AB_2292909
rabbit anti-Synapsin1 (A30)	Abcam	Cat#: ab8; RRID: AB_2200097
guinea pig anti-Synaptophysin (A106)	Synaptic Systems	Cat#:101 004; RRID: AB_1210382
guinea pig anti-vGlut1 (A50)	Synaptic Systems	Cat#:135 304; RRID: AB_887878
rabbit anti-MAP2 (A139)	Synaptic Systems	Cat#:188 002; RRID: AB_2138183
mouse anti-MAP2 (A108)	Sigma-Aldrich	Cat#:M4403; RRID: AB_477193
mouse anti-β-actin (A127)	Sigma-Aldrich	Cat#: A5316; RRID:AB_476743
mouse anti-HA (A12)	Biolegend	Cat#:901501; RRID: AB_2565006
Bacterial and Virus Strains		
AAV8-EF1a-mCherry-IRES-Cre	Fenno et al., 2014, Addgene	Cat#: 55632-AAV8; RRID: Addgene_55632
Chemicals, Peptides, and Recombinant Proteins		
ω-Agatoxin IVA	Alomone labs	Cat#: STA-500
ω-Conotoxin GVIA	Alomone labs	Cat#: C-300
Tetrodotoxin (TTX)	Tocris Bioscience	Cat#: 1078
γ-D-Glutamylglycine (γ-DGG)	Tocris Bioscience	Cat#: 0112
Picrotoxin	Tocris Bioscience	Cat#: 1128
D-amino-5-phosphonopentanoic acid (D-AP5)	Tocris Bioscience	Cat#: 0106
6-Cyano-7-nitroquinoxaline-2,3-dione (CNQX)	Tocris Bioscience	Cat#: 0190
QX314-Cl	Tocris Bioscience	Cat#: 2313
Experimental Models: Cell Lines		
HEK293T cells	ATCC	Cat#: ATCC CRL-3216; RRID:CVCL_0063

(*Continued on next page*)

Continued

REAGENT or RESOURCE	SOURCE	IDENTIFIER
Experimental Models: Organisms/Strains		
Mouse: Cacna1a conditional knockout	Todorov et al., 2006	N/A
Mouse: Cacna1b$^{tm1a(KOMP)Wtsi}$	IMPC	Cat# KOMP: CSD34514; RRID: IMSR_KOMP: CSD34514-1a-Wtsi
Mouse: Cacna1e conditional knockout	Pereverzev et al., 2002	N/A
Mouse: Cacna2d1$^{tm1.1Gfng}$ /J	Park et al., 2016-, gift from Drs. G. Feng and C. Dulla	RRID: IMSR_JAX:030704
Mouse: 129S2/SvPasCrl	Charles River	RRID:IMSR_CRL:287
Recombinant DNA		
pCMV HA-CaV2.1 (p771)	this study	N/A
pCMV HA-CaV2.1 ΔL_{1775}-C_{2368} (CaV2.1-ΔCt, p784)	this study	N/A
pCMV HA-CaV2.1 Δ2365-2368 (CaV2.1$^{\Delta P}$, p785)	this study	N/A
pCMV HA-CaV2.1 $_{2239}$AxxA$_{2242}$ (CaV2.1^{AxxA}, p779)	this study	N/A
pCMV HA-CaV2.1 Δ2016-2060 (CaV2.1$^{\Delta K}$, p787)	this study	N/A
pCMV HA-CaV2.1 Δ2365-2368 + $_{2239}$AxxA$_{2242}$ (CaV2.1$^{\Delta P+AxxA}$, p780)	this study	N/A
pCMV HA-CaV2.1 Δ2365-2368 + Δ2016-2060 (CaV2.1$^{\Delta P+\Delta K}$, p782)	this study	N/A
pCMV HA-CaV2.1 $_{2239}$AxxA$_{2242}$ + Δ2016-2060 (CaV2.1$^{AxxA+\Delta K}$, p778)	this study	N/A
pCMV HA-CaV2.1 Δ2365-2368 + $_{2239}$AxxA$_{2242}$ + Δ2016-2060 (CaV2.1 $^{\Delta P+AxxA+\Delta K}$, p781)	this study	N/A
pFSW HA-CaV2.1 (p789)	this study	N/A
pFSW HA-CaV2.1 ΔL_{1775}-C_{2368} (CaV2.1-ΔCt, p784)	this study	N/A
pFSW HA-CaV2.1 Δ2365-2368 (CaV2.1$^{\Delta P}$, p785)	this study	N/A
pFSW HA-CaV2.1 $_{2239}$AxxA$_{2242}$ (CaV2.1^{AxxA}, p779)	this study	N/A
pFSW HA-CaV2.1 Δ2016-2060 (CaV2.1$^{\Delta K}$, p787)	this study	N/A
pFSW HA-CaV2.1 Δ2365-2368 + $_{2239}$AxxA$_{2242}$ (CaV2.1$^{\Delta P+AxxA}$, p780)	this study	N/A
pFSW HA-CaV2.1 Δ2365-2368 + Δ2016-2060 (CaV2.1$^{\Delta P+\Delta K}$, p782)	this study	N/A
pFSW HA-CaV2.1 $_{2239}$AxxA$_{2242}$ + Δ2016-2060 (CaV2.1$^{AxxA+\Delta K}$, p778)	this study	N/A
pFSW HA-CaV2.1 Δ2365-2368 + $_{2239}$AxxA$_{2242}$ + Δ2016-2060 (CaV2.1 $^{\Delta P+AxxA+\Delta K}$, p781)	this study	N/A
pMT2 CaV β1b-GFP (p754)	Page et al., 2016, Addgene	Cat#: 89893; RRID: Addgene_89893
pCDNA3.1 CaV α2δ-1 (p752)	Lin et al., 2004, Addgene	Cat#: 26575; RRID: Addgene_26575
Software and Algorithms		
Prism	Graphpad software	RRID:SCR_002798; v8.3.0 https://www.graphpad.com/scientific-software/prism/
Fiji	Schindelin et al., 2012	RRID:SCR_002285; https://imagej.net/Fiji/Downloads

(*Continued on next page*)

Continued

REAGENT or RESOURCE	SOURCE	IDENTIFIER
pClamp	Molecular Devices	RRID: SCR_011323; v10.7.0.3
Igor Pro	Wavematrics	RRID:SCR_000325; v6.37 https://www.wavemetrics.com/downloads
MATLAB	Mathworks	RRID: SCR_001622; https://www.mathworks.com/products/matlab.html

RESOURCE AVAILABILITY

Lead Contact

Further information and requests for resources and reagents should be directed to and will be fulfilled by the Lead Contact, Pascal S. Kaeser (kaeser@hms.harvard.edu).

Materials Availability

Plasmids generated for this study will be shared without restrictions. Antibodies generated for this study are exhaustible and will be shared as long as they are available. Mouse lines will be shared upon request within the limits of the respective material transfer agreements.

Data and Code Availability

This study did not generate datasets or code.

EXPERIMENTAL MODEL AND SUBJECT DETAILS

All animal experiments were performed according to institutional guidelines at Harvard University. Mice were group-housed with free access to water and food and experiments were performed with animals of both sexes. For hippocampal neuronal culture, postnatal day 0 (P0) pups were used to generate cultures and cultures were used for experiments at DIV15-19. For calyx of Held experiments, animals were sacrificed at P13-16. $Ca_V2.2$ (*Cacna1b*) gene-trap knockout mice were obtained from the IMPC (IMSR Cat# KOMP: CSD34514-1a-Wtsi, RRID: IMSR_KOMP: CSD34514-1a-Wtsi) and crossed to transgenic mice expressing Flp recombinase (Dymecki, 1996) to remove the LacZ/Neomycin cassette and to generate a conditional knockout allele with LoxP sites flanking exons 5 and 6. Conditional triple knockout (cTKO) mice for simultaneous ablation of $Ca_V2.1$, $Ca_V2.2$, and $Ca_V2.3$ proteins were generated by crossing conditional *Cacna1a* (Todorov et al., 2006), *Cacna1b* (described above), and *Cacna1e* (Pereverzev et al., 2002) mice. Ca_V2 cTKO mice were maintained as triple homozygote line. Conditional $\alpha2\delta$-1 knockout mice, described in Park et al. (2016), were obtained from Dr. Chris Dulla with permission of Dr. Guoping Feng.

METHOD DETAILS

Cell culture and lentiviral infection

Primary mouse hippocampal cultures were generated from newborn pups as previously described (Liu et al., 2014; Wang et al., 2016). Newborn pups were anesthetized on ice slurry within 24 h after birth and the hippocampus was dissected out. Cells were dissociated and plated onto glass coverslips in tissue culture medium composed of Mimimum Essential Medium (MEM) with 0.5% glucose, 0.02% $NaHCO_3$, 0.1 mg/mL transferrin, 10% Fetal Select bovine serum (Atlas Biologicals FS-0500-AD), 2 mM L-glutamine, and 25 μg/mL insulin. Cultures were maintained in a 37°C tissue culture incubator, and after ~1 day the plating medium was exchanged with growth medium composed of MEM with 0.5% glucose, 0.02% $NaHCO_3$, 0.1 mg/mL transferrin, 5% Fetal Select bovine serum (Atlas Biologicals FS-0500-AD), 2% B-27 supplement (Thermo Fisher 17504044), and 0.5 mM L-glutamine. At DIV3 or DIV4 (depending on cell growth), 50% of the medium was exchanged with growth medium supplemented with 4 μM Cytosine β-D-arabinofuranoside (AraC) to inhibit glial cell growth. Lentiviruses expressing EGFP-tagged cre recombinase (to generate knockout neurons) or a truncated, enzymatically inactive EGFP-tagged cre protein (to generate control neurons) were produced in HEK293T cells by Ca^{2+}-phosphate transfection. Expression in all lentiviral constructs was driven by the human Synapsin promoter to restrict expression to neurons (Liu et al., 2014; Wang et al., 2016). If not otherwise noted, neurons were infected with HEK293T cell supernatant at DIV5 as described before (Liu et al., 2014; Wang et al., 2016) and experiments were performed at DIV15-19. For rescue expression with HA-tagged $Ca_V2.1$ and with $Ca_V2.1$ mutants, neurons were infected at DIV1 with rescue virus and with cre/control virus at DIV5. The $Ca_V2.1$ rescue cDNA was from mouse and is identical to GenBank: AAW56205.1. All residue numbering in the text and figures reference NCBI RefSeq: NP_031604.3 which matches the full-length mouse genome (Ensembl ENSMUST00000121390.7).

Electrophysiological recordings from neurons

Electrophysiological recordings in cultured hippocampal neurons were performed as described (Liu et al., 2014; Wang et al., 2016) at DIV15-19. The extracellular solution contained (in mM): 140 NaCl, 5 KCl, 1.5 $CaCl_2$, 2 $MgCl_2$, 10 Glucose, 10 HEPES-NaOH (pH 7.4, ~310 mOsm). Glass pipettes were pulled at 2 - 4 MΩ and filled with intracellular solutions listed below for each experiment. Recordings were preformed at room temperature (21-24°C), and access resistance was monitored during recording and cells were discarded if access exceeded 15 MΩ or 20 MΩ during recording of evoked or spontaneous synaptic currents, respectively. Access resistance was compensated to 3-5 MΩ during recording. A bipolar focal stimulation electrode made from nichrome wire was used to evoke action potentials. For superfusion of cells with hyperosmotic sucrose solutions, a syringe pump was used to apply extracellular solution supplemented with sucrose to a final osmolarity of 800 mOsm (500 mOsm hypertonic from standard). Sucrose solution was applied at a flow rate of 10 μL/min for 10 s through a tip with an inner diameter of 250 μm.

Inhibitory postsynaptic currents (IPSCs) were isolated pharmacologically with D-amino-5-phosphonopentanoic acid (D-APV, 50 μM) and 6-Cyano-7-nitroquinoxaline-2,3-dione (CNQX, 20 μM) added to the extracellular solution. Intracellular solution contained (in mM): 40 CsCl, 90 K-Gluconate, 1.8 NaCl, 1.7 MgCl2, 3.5 KCl, 0.05 EGTA, 2 MgATP, 0.4 Na2-GTP, 10 Phosphocreatine, 4 QX314-Cl, 10 HEPES-CsOH (pH 7.4, ~300 mOsm). Cells were kept at a holding potential of −70 mV throughout the recording. To test blocker sensitivity in Figures S1C–S1F, IPSCs were continuously recorded at 0.067 Hz, and blockers (ω-conotoxin GVIA (ω-Ctx, 250 nM) in S1C and S1D, ω-Agatoxin IVA (ω-Aga, 200 nM) in S1E and S1F) were added to the recording chamber in 0.25% BSA after 3.5 min (15 stimuli) when the initial IPSC amplitude was stable. After toxin wash on, IPSCs were recorded for an additional 6 min, or until the response amplitude stabilized. IPSC amplitudes were normalized to the last five IPSCs before toxin addition. Example traces show averages of these five IPSCs (black trace) and of the average of the final five IPSCs (red trace).

Excitatory postsynaptic currents (EPSCs) carried by AMPA receptors were isolated using D-APV (50 μM) and Picrotoxin (PTX, 50 μM) added to the extracellular solution. For mEPSC recordings and sucrose evoked responses, tetrodotoxin (TTX, 1 μM) was added in addition to block action potentials. For evoked EPSC recordings, 1 mM γ-D-Glutamylglycine (γ-DGG) was also added to the bath to block AMPA receptor saturation, which also reduced the overall excitation and reverberant activity that is present upon stimulation (Liu et al., 2014; Wang et al., 2016). Intracellular solution contained (in mM): 120 Cs-methanesulfonate, 10 EGTA, 2 $MgCl_2$, 4 Na_2-ATP, 1 Na_2-GTP, 4 QX314-Cl, 10 HEPES-CsOH (pH 7.4, ~300 mOsm). Cells were kept at a holding potential of −70 mV. EPSCs carried by NMDA receptors were isolated using 20 μM CNQX and 50 μM PTX. Intracellular solutions contained (in mM): 120 Cs-methanesulfonate, 10 EGTA, 2 $MgCl_2$, 4 Na_2-ATP, 1 Na_2-GTP, 4 QX314-Cl, 10 HEPES-CsOH (pH 7.4, ~300 mOsm). After breaking into the cell and establishing the whole-cell recording configuration cells were held at +40 mV for the recording of NMDAR-mediated currents. To generate the time-course of NMDAR-mediated synaptic transmission in Figures S4A and S4B, cultures were infected with lentivirus on DIV5 and NMDA-EPSCs were evaluated every 2 days starting from DIV5 until DIV17.

Data acquisition was performed with an Axon 700B Multiclamp amplifier and digitized with a Digidata 1440A digitizer. All data acquisition and analysis were done using pClamp10. Quantification of peak amplitudes was performed by subtracting any baseline current and finding the negative or positive peak of the response following the stimulus artifact. For analyses of train-evoked responses, 50 stimuli were provided at a frequency of 10 Hz. Individual IPSCs within the train were aligned using the peak of the stimulus artifact and the baseline value set to the negative peak immediately following the artifact. Peak amplitudes were determined using these aligned events. The readily releasable pool (RRP) was quantified by integrating the total charge transfer during the first 10 s of the sucrose evoked response. mEPSC and mIPSC frequency were determined by counting the total number of events during a three min recording window. mEPSC and mIPSC amplitudes were measured on a per-cell basis by aligning and averaging all events for an individual cell and finding the peak of the averaged event. For all electrophysiological experiments, the experimenter was blind to the genotype throughout data acquisition and analyses.

Electrophysiological recordings from HEK293T cells

For recordings in HEK293T cells, the cells were first plated on matrigel-coated glass coverslips (12 mm in diameter) at 10%–20% confluency. 12-24 h later, the $Ca_V2.1$ expression vectors (in pCMV, HA-tagged) were cotransfected with pMT2-β1b-GFP and pcDNA-α2δ-1 (a total 1 μg of DNA per coverslip was used with molar ratio 1:1:1, or 0.67 μg/coverslip with molar ratio 1:1 if pcDNA-α2δ-1 was absent) using Ca^{2+} phosphate transfection, and in Figures S6I–S6K a soluble mVenus (in pCMV, 0.05 μg) was co-transfected in all conditions. All comparisons were done such that each transfection contained a $Ca_V2.1$ control and typically two mutants in random order. Hence, some control $Ca_V2.1$ experiments are shared across mutants, but each mutant has a unique combination of controls that were recorded on the same day. Ba^{2+} current recordings were carried out 36-48 h after transfection at room temperature (21-24°C) as previously described (Kaeser et al., 2012). Briefly, the coverslips were transferred to extracellular solution containing (in mM): 10 $BaCl_2$, 140 mM TEA-Cl, 10 HEPES and 10 glucose (pH 7.4 with TEA-OH). Glass pipettes were pulled at 2 - 4 MΩ and filled with intracellular solution containing (in mM): 135 Cs-methanesulfonate, 5 CsCl, 0.5 EGTA, 5 $MgCl_2$, 4 Na_2-ATP, and 10 HEPES (pH 7.2 with CsOH). Whole cell recording was performed on cells with robust GFP expression, judged as expression above the mean of the transfected cells by an experimenter blind to the condition. Cells were held at −80 mV for at least 5 mins before recording and discarded if the access resistance exceeded 15 MΩ during recording, and voltage step protocols were applied as indicated in each figure. For I-V and activation curves, Ba^{2+} currents were evoked by 50 ms depolarizations from −50 mV to +50 mV at 10 mV increments every 10 s. The peaks of the currents during the depolarization and tail currents immediately after the depolarizations were measured for generating I-V and activation curves, respectively. For testing inactivation, cells were stimu-

lated every 20 s. A 2 s long depolarization from −80 mV to +50 mV (10 mV increments) was first applied. Subsequently, the holding potential was switched to +5 mV for 10 ms after the depolarization, and the peak Ba^{2+} current at +5 mV was measured for generating the inactivation curve. For all electrophysiological experiments, P/4 leak subtraction was used and no resistance compensation was applied. For all HEK293T cell recordings, the experimenter was blind to the genotype throughout data acquisition and analyses. pMT2 Beta1b GFP was a gift from Annette Dolphin obtained through Addgene (plasmid # 89893; http://addgene.org/89893 ; RRID:Addgene_89893). pcDNA3.1 CaV α2δ-1 was a gift from Diane Lipscombe obtained through Addgene (plasmid # 26575; http://addgene.org/26575 ; RRID:Addgene_26575).

Electrophysiological recordings at the calyx of Held

To remove Ca_V2s from the calyx of Held synapse *in vivo*, adeno-associated virus (pAAV-Ef1a-mCherry-IRES-Cre (Fenno et al., 2014), a gift from Karl Deisseroth obtained through Addgene, #55632-AAV8) for co-expression of cytosolic mCherry and cre recombinase (Figure 5A) were injected into brains of newborn mice. Mice were deeply anesthetized on ice slurry. A syringe needle (200 μm in diameter) was then lowered into the anterior ventral cochlear nucleus (AVCN) through the ear, and the virus was delivered at a speed of 1 μL/min for a total volume of 1 μL. After recovery from the surgery, the mice were returned to their home cage, monitored, and used for recording at P13-P16. The virus was injected either into Ca_V2 triple floxed mice (to generate Ca_V2 cTKO) or into wild-type mice (129SvPasCrl, to generate Ca_V2 controls). For electrophysiological recordings, mice (postnatal day 13-16) were deeply anesthetized using isoflurane and decapitated. Coronal brain slices containing the medial nucleus of the trapezoid body (MNTB, 200 μm thick) were then prepared using a vibratome (Leica, VT1200s) in ice-cold slicing solution containing (in mM): 125 NaCl, 2.5 KCl, 0.1 $CaCl_2$, 3 $MgCl_2$, 25 $NaHCO_3$, 1.25 NaH_2PO_4, 25 glucose 3 Myo-inositol, 2 Na-pyruvate, 0.4 ascorbic acid, continuously bubbled with 95% O2 and 5% CO2. After cutting, the slices were incubated at 37°C for 30 min in artificial cerebrospinal fluid (ACSF) containing (in mM): 25 NaCl, 2.5 KCl, 2 $CaCl_2$, 1 $MgCl_2$, 25 $NaHCO_3$, 1.25 NaH_2PO_4, 25 glucose 3 Myo-inositol, 2 Na-pyruvate, 0.4 ascorbic acid, continuously bubbled with 95% O_2 and 5% CO_2 and then transferred to room temperature. For whole-cell EPSC recordings, the slices were perfused in ACSF containing 50 μM picrotoxin at 30°C, and the recordings were performed only on principle neurons with robust mCherry expression in the corresponding calyx, judged visually as expression above the mean of the transduced calyces. Patch pipettes filled with internal solution containing (in mM): 120 Cs-methanesulfonate, 10 EGTA, 2 $MgCl_2$, 4 Na_2-ATP, 1 Na_2-GTP, 4 QX-314, 10 HEPES-CsOH (pH 7.4) with serial resistance of 2-4 MΩ were used. After whole-cell configuration, the cells were held at −80 mV, and the serial resistance was compensated to 2-3 MΩ during the recording. For evoking presynaptic action potentials, a parallel bipolar electrode (made of platinum-iridium, 125 μm in probe diameter, separated by 0.5 mm) was placed between the midline of the brainstem and the MNTB region. Biphasic stimuli (500-700 μA, duration of 0.5 ms) were applied every 10 s. To exclude recordings from calyx of Held synapses in which fiber stimulation did not trigger action potentials, only cells with an EPSC bigger than 10 pA were included in the analyses shown in Figures 5C–5F. 31% of control and 60% of cTKO calyces failed to meet these criteria.

Presynaptic Ca^{2+} Imaging

Ca^{2+} imaging experiments were performed as previously described (Held et al., 2016; Liu et al., 2014). Briefly, Ca^{2+} transients were recorded in neurons at DIV15-18 in extracellular solution containing (in mM): 140 NaCl, 5 KCl, 2 $CaCl_2$, 2 $MgCl_2$, 10 Glucose, 0.05 APV, 0.02 CNQX, 0.05 PTX, 10 HEPES (pH 7.4, NaOH). Patch pipettes were pulled and filled with solution containing (in mM): 140 K Gluconate, 0.1 EGTA, 2 $MgCl_2$, 4 Na_2-ATP, 1 Na_2-GTP, 0.3 Fluo5F, 0.03 Alexa Fluor 594, 10 HEPES (pH 7.4, KOH). Whole-cell recordings were performed at room temperature, and neurons with resting potentials higher than −55 mV were discarded. A holding current was injected to keep the membrane potential at −60 mV. After loading the cell with the intracellular solution for 10 min, the axon with presynaptic boutons was identified in the red channel based on the bead-like morphology and an image was acquired. Ca^{2+} transients were triggered by a single action potential induced by a brief somatic current injection (5 ms, 1000-1500 pA). Fluorescent signals were excited by a light-emitting diode at 470 nm, collected with a 60X, 1.0 numerical aperture water immersion objective, and acquired using a scientific complementary metal–oxide–semiconductor camera (sCMOS, Hamamatsu orca flash4.0) at 100 frames/s. Images were acquired for 200 ms before and 1 s after the initiation of action potential. The total time of filling, recording and imaging per cell was 15-20 min. Ca^{2+} transients were quantified using ImageJ. 7-20 boutons of each neuron were randomly selected from the image taken in the red channel. After background subtraction (rolling ball method with a radius of 2 μm), the $(F-F_0)/F_0$ in the green channel in each bouton was calculated (F = fluorescence intensity at a given frame, F_0 = average fluorescence intensity before action potential induction). A time-course was calculated for each bouton and averaged for comparison. For all Ca^{2+} imaging experiments comparing Ca_V2 control and cTKO neurons, the experimenter was blind to the genotype throughout data acquisition and analyses.

To test the sensitivity of leftover Ca^{2+} transients in Ca_V2 cTKO boutons to Ca^{2+} channel blockers (Figure S2E), 5 action potentials were evoked in the presence of 4 mM extracellular Ca^{2+} to enhance the Ca^{2+} transients, and drug effects were evaluated 10-15 min after drug addition. ω-conotoxin GVIA (ω-Ctx, 250 nM) and ω-Agatoxin IVA (ω-Aga, 200 nM) were added to the recording chamber in 0.25% BSA on top of nimodipine (15 μM).

Electron microscopy

For high-pressure freezing, neurons cultured on 6 mm carbon-coated sapphire coverslips were frozen using a Leica EM ICE high-pressure freezer in extracellular solution containing (in mM): 140 NaCl, 5 KCl, 2 $CaCl_2$, 2 $MgCl_2$, 10 HEPES-NaOH (pH 7.4), 10 Glucose (~310 mOsm) with PTX (50 μM), D-AP5 (50 μM), and CNQX (20 μM) added to block synaptic transmission. After freezing, samples were first freeze-substituted in 1% glutaraldehyde, 1% osmium tetroxide, 1% water, and anhydrous acetone with the following protocol: −90°C for 5 h, 5°C per h to −20°C, −20°C for 12 h, and 10°C per h to 20°C (AFS2, Leica). Following freeze substitution, samples were Epon infiltrated, and baked for 24 h at 60°C before sectioning at 50 nm and imaging. Images of single or serial sections were taken with a transmission electron microscope (JEOL 1200 EX at 80 kV accelerating voltage) and processed with ImageJ. The total number of vesicles, the number of docked vesicles, the length of the PSD, the area of the presynaptic bouton, and the distance of each vesicle from the active zone were analyzed in each section using a custom-written MATLAB code. Bouton size was calculated from the measured perimeter of each synapse. Docked vesicles were defined as vesicles touching the presynaptic plasma membrane opposed to the PSD such that the density of the two membranes was not visually separable. Data in Figures S2A–S2C were quantified directly from single sections. Data in Figures 2A–2D were obtained from reconstructed 3D synapses of a separate set of images. For 3D-EM reconstruction and quantification, the samples were first prepared using the same method as described above. Serial sections (50 nm) of the same synapse were then sequentially cut and imaged. The position and orientation information of vesicles and active zones were first extracted from each layer using SynapseEM and then used for 3D-reconstruction in MATLAB. Some synapses had perforated PSDs (2/12 for Ca_V2 control, 3/13 Ca_V2 cTKO). If the PSD was perforated, the area of perforation was not included in the measurement of PSD size, but for assessing vesicle docking the corresponding area on the presynaptic cell was considered part of the active zone area. All experiments and analyses were performed by an experimenter blind to the genotype.

Generation of custom antibodies

Custom antibodies against $Ca_V2.2$ were generated in rabbits against a small $Ca_V2.2$ peptide (sequence: RHHRHRDRDKTSATAPA, located in II-III intracellular loop) conjugated to keyhole lympet hemocyanin (KLH). KLH-conjugated peptides were injected into rabbits, for which the sera had been pre-screened to avoid non-specific antibody signal. Rabbits were given a booster every 2 weeks and bleeds were taken every 3 weeks. Each bleed was tested for immunoreactivity to $Ca_V2.2$ using western blots of samples from brain homogenates. The serum with the highest immunoreactivity (antibody 1089, bleed 5, A37) was affinity purified with the original peptide antigen.

Western blotting

Western blotting was performed using standard protocols using SDS-PAGE gels and nitrocellulose transfer membranes. Coverslips were harvested in 1X SDS sample buffer with 1 μL benzonase/50 μL sample buffer included. Samples were frozen in dry-ice/ethanol then thawed in a 37°C water bath 3-5 times. To prevent the formation of higher order aggregates of Ca_V2s, samples were not boiled prior to loading on the gel for all Ca_V2 western blotting. The following antibodies were used for blotting: rabbit anti-$Ca_V2.2$ (1:200, custom made, this paper, A37), mouse monoclonal anti-α2δ−1 (1:500, RRID:AB_1078663, A174), and monoclonal mouse anti-β-actin (1:2000, RRID:AB_476743, A127). HRP-conjugated secondary antibodies, a standard chemiluminescent agent, and exposure to film were used for visualization.

STED imaging

For STED imaging, neurons were cultured on 0.17 mm (#1.5) thick coverslips. Before all antibody staining, they were washed two times with warm PBS, and then fixed for 10 min in 4% PFA + 4% sucrose (in PBS) unless otherwise noted. For staining with $Ca_V2.1$, $Ca_V2.2$ and α2δ-1 antibodies, cultures were fixed for 10 min in 2% PFA + 4% sucrose (in PBS) since mild fixation was found to improve Ca_V2 labeling. Following fixation, coverslips were rinsed twice in PBS + 50 mM glycine and blocked/permeabilized in PBS + 0.1% Triton X-100 + 3% BSA (TBP) for 1 h. Primary antibodies were diluted in TBP and coverslips were stained overnight at 4°C. The following primary antibodies were used: Monoclonal mouse anti-$Bassoon^N$ (N-terminal, 1:1000, RRID: AB_11181058, A85), guinea pig anti-$Bassoon^C$ (C-terminal, 1:1000, RRID: AB_2290619, A67), monoclonal mouse anti-PSD-95 (1: 200, RRID: AB_10698024, A149), rabbit anti-Synapsin 1 (1:1000, RRID: AB_2200097, A30), rabbit anti-$Ca_V2.1$ (1:200, RRID: AB_2619841, A46), rabbit anti-$Ca_V2.2$ (1:200, custom made, this paper, A37), rabbit anti-RIM1 (1:1000, RRID: AB_887774, A58), rabbit anti-RIMBP2 (1:1000, RRID: AB_2619739, A126), rabbit anti-Liprin-α3 (serum 4396, 1:5000, gift from Dr T. Südhof, A35), anti-ELKS2α (serum E3-1029, 1:100, custom made, A136, (Held et al., 2016)), rabbit anti-Munc13-1 (1:1000, RRID: AB_887733, A72), rabbit anti-α2δ-1 (1:500, AB_2039785, A133), guinea pig anti-vGlut1 (1:500, RRID: AB_887878, A50), and mouse monoclonal anti-HA (1:250, RRID: AB_2565006, A12). After primary antibody staining, coverslips were rinsed twice and washed 3-4 times for 5 min in TBP. Alexa Fluor 488, 555, and 633 conjugated secondary antibodies were used as secondary antibodies at 1:200 (488 and 555) or 1:500 (633) dilution in TBP. Secondary antibody staining was done overnight at 4°C followed by rinsing two times and washing 3-4 times 5 min in TBP. Stained coverslips were post-fixed for 10 min with 4% PFA + 4% sucrose in PBS, rinsed two times in PBS + 50 mM glycine, then once in deionized water, air-dried and mounted on glass slides.

STED images were acquired with a Leica SP8 Confocal/STED 3X microscope with an oil immersion 100X 1.44 numerical aperture objective and gated detectors as described in Wong et al. (2018). 46.51 × 46.51 μm^2 areas were selected as ROIs and were scanned at a pixel density of 4096 × 4096 (11.4 nm/pixel). Alexa Fluor 633, Alexa Fluor 555, and Alexa Fluor 488 were excited with 633 nm,

555 nm and 488 nm using a white light laser at 2%–5% of 1.5 mW laser power. The Alexa Fluor 633 channel was acquired first in confocal mode using 2X frame averaging. Subsequently, Alexa Fluor 555 and Alexa Fluor 488 channels were acquired in STED mode, depleted with 660 nm (35% of max power, 35% axial depletion) and 592 nm (80% of max power, 30% axial depletion) depletion lasers, respectively. Line accumulation (4-10x) and frame averaging (2x) were applied during STED scanning. Identical settings were applied to all samples within an experiment.

For quantification of PSD-95 in STED images, the PSD-95 puncta were detected using automatic two-dimensional segmentation (Otsu algorithm) with a size filter of 0.04-0.4 μm^2 without considering the shape or orientation of the signal. The intensity and size distribution of the detected objects were averaged for each image and plotted.

For all analyses of other proteins in STED images, side-view synapses were defined as synapses that contained a synaptic vesicle cluster, defined by a synaptic vesicle marker (VGluT1, synapsin or synaptophysin as indicated in figures) with an elongated PSD-95 structure along the edge of the vesicle cluster as described (de Jong et al., 2018; Wong et al., 2018). For intensity profile analyses, side-view synapses were selected using only the PSD-95 signal and the vesicle signal for all figures except Figure S8 (for which Bassoon^N was used), and we have previously established that these intensity measurements correlate well with analyses of synaptic fluorescence intensities in confocal microscopy (Wong et al., 2018). An ROI was manually drawn around the PSD-95 signal and fit with an ellipse to determine the center position and angle from normal. A 1306 nm long, 227 nm wide rectangle was then drawn using these coordinates, selected perpendicular to the elongated PSD-95 structure across its center. An intensity profile was obtained for all three channels along this region. To align individual profiles, the PSD-95 signal was first smoothed using a moving average of 5 pixels, and the smoothed signal was used to define the position of the peak. All three channels (vesicle marker, test protein, non-smoothed PSD-95) were then aligned to this peak position and averaged across images. For Figure S8, identical procedures were used, but Bassoon^N was used instead of PSD-95. For long-term blockade of Ca^{2+} entry in Figure 4, 200 nM ω-Agatoxin IVA and 250 nM ω-conotoxin GVIA with or without 1 μM TTX were added to the culture every three days starting from 12 h after plating until DIV15. Cultures were washed once with PBS and fixed on DIV15 using 4% PFA (in PBS), and staining and imaging were performed as in all other conditions. To ensure that the drug supplemented media was sufficient to fully block action potential triggered neurotransmitter release throughout the culture period, cell culture supernatant was collected at DIV15 and stored in the incubator for 3 additional days. Using independent cultures grown without blockers, we recorded action potential evoked NMDAR-EPSCs and drug supplemented supernatant was diluted into extracellular solution to 20% of the final volume. Both media containing Ca_V2 blockers only and media containing Ca_V2 blockers + TTX eliminated the evoked EPSCs (not shown), indicating that the toxins are stable during incubation. All analyses were performed on raw images without background subtraction or adjustments and were done identically for all experimental conditions. Representative images were brightness and contrast adjusted to facilitate inspection, and these adjustments were made identically for images within an experiment. The experimenter was blind to the condition/genotype for all image acquisition and analyses.

3D STORM imaging

Hippocampal cultures for 3D dSTORM experiments were grown on Matek dishes. They were washed two times with warm PBS, and then fixed for 10 min in 4% PFA + 4% sucrose (in PBS). Following fixation, dishes were rinsed twice in PBS + 50 mM glycine and blocked/permeabilized in 3% BSA or 5% serum in PBS/Glycine with 0.2% Triton X-100 for 1 h at room temperature. Primary antibodies were diluted in 3% BSA and 0.05% Triton (in PBS) and dishes were stained overnight at 4°C. The following primary antibodies were used: monoclonal mouse anti-PSD-95 (1: 200, RRID: AB_2292909), rabbit anti-RIM1 (1:500, RRID: AB_887774, A58). After primary antibody staining, coverslips were rinsed twice and washed 3-4 times for 5 min in PBS/Glycine. Donkey anti-Rabbit Alexa647 (1:200) and donkey anti-Mouse CF555 (1:500) were used as secondary antibodies, diluted in 3% BSA and 0.05% Triton (in PBS). Staining was done for 3 h at room temperature, followed by washing 3-4 times for 5 min in PBS/Glycine. Stained coverslips were post-fixed for 1 h with 4% PFA + 2% sucrose in PBS then washed two times in PBS/Glycine. The stained cultures were then shipped to the University of Maryland, where 3D dSTORM imaging was carried out essentially as described (Tang et al., 2016) on an Olympus IX81 ZDC2 inverted microscope with a 100X/1.49 TIRF oil-immersion objective. The incident angle of the excitation beam was adjusted to achieve oblique illumination of the sample to reduce background fluorescence. Emission was passed through a Photometrics DV2, which split the emission at 565 nm and directed through red and far-red emission filters onto an iXon+ 897 EM-CCD camera (Andor). An adaptive optics device (MicAO, Imagine Optics) was used to correct optical aberrations and achieve astigmatism for 3D imaging. Image acquisition was controlled via iQ software (Andor). Stability in the Z-dimension was maintained using the Olympus ZDC2 feedback positioning system, and lateral drift was corrected post hoc using a cross-correlation drift correction. TetraSpeck beads (100 nm; Invitrogen) embedded in 5% agarose were localized to correct alignment between the two channels as described previously (MacGillavry et al., 2013). The average deviation of the bead localizations after correction was between 10 and 15 nm. For the 3D positions of localizations, a z-stack with 20 nm steps was collected from the same beads embedded in agarose at a depth that matched that of the cells being imaged (~2-5 μm). Cells were imaged in imaging buffer containing 50 mM Tris, 10 mM NaCl, 10% glucose, 0.5 mg/mL glucose oxidase (Sigma), 40 μg/mL catalase (Sigma), and 0.1 M cysteamine (Sigma). The multi-color 3D dSTORM analysis workflow was carried out using custom routines in MATLAB (Mathworks). Molecule localization and filtering was performed as previously described (Tang et al., 2016). Putative synapses could be identified as juxtaposed clusters of localizations from the labeled molecule pair when all detected localizations were displayed as a 2D scatterplot. Synapses for analysis were then manually selected based on several criteria. To achieve an unbiased viewpoint when representing synapses in 3D, a plane rep-

resenting the synaptic cleft was determined from the best fit to the localizations from both channels of the putative synapse. Structures in which the peak-to-peak distance of RIM1 to PSD-95 distributions was less than 50 or greater than 180 nm that extended outside of the z range of the imaged volume, or that had a synaptic cluster volume less than 2×10^{-3} or greater than 30×10^{-3} μm^3 were eliminated from further analysis.

The 3D paired cross-correlation function $g_c(r)$ was calculated as described previously (Tang et al., 2016). The function calculates the cross-correlation between two matrices constructed from localization density in the two image channels. The calculation normalizes for the synaptic cluster shape and mean molecule density, such that $g_c(r) > 1$ indicates similarity in the organization of the measured localizations between the two channels at lateral separation r. However, $g_c(r)$ approaches 1 if the internal organization of one channel is randomly distributed or the two distributions are spatially unrelated, and can be < 1 if molecules are de-enriched across from one another.

Within each synaptic cluster, nanoclusters were identified if they contained $\geq$ 4 localizations whose ranked local density exceeded a threshold identified to reduce false-positive detection (Chen et al., 2020; Tang et al., 2016). Local peaks within a cutoff distance were considered a single nanocluster based on a further sub-classification of those nanoclusters, where the distance cutoff of 80 nm was based on prior auto-correlation analyses. Enrichment profiles were calculated essentially as described (Chen et al., 2020; Tang et al., 2016) by measuring the angularly averaged density of localizations within the synaptic cluster border as a function of the distance from the center of nanoclusters in the same or opposite channel, and normalized to the expected density based on the total localizations measured in the synapse. This expected density was calculated via a randomized distribution of points in the synapse using the average density of the synaptic cluster, thus accounting for the individual geometry of each synapse. Enrichment profiles were calculated per nanocluster, not per synapse.

All dSTORM experiments were performed and analyzed by an experimenter blind to genotype.

Confocal imaging in cultured neurons

Cultured neurons grown on glass coverslips were washed two times with warm PBS, then fixed for 10 min in 4% PFA + 4% sucrose (in PBS). Following fixation coverslips were rinsed twice in PBS, then blocked/permeabilized in PBS + 0.1% Triton X-100 + 3% BSA (TBP) for 1 h. Primary antibodies were diluted in TBP and coverslips were stained overnight at 4°C. The following primary antibodies were used for confocal imaging: guinea pig anti-Synaptophysin (1:500, RRID: AB_1210382, A106), rabbit anti-MAP2 (1:500, RRID: AB_2138183, A139), monoclonal mouse anti-MAP2 (1:500, RRID: AB_477193, A108), mouse monoclonal anti-$Ca_V\beta1$ (1:50, RRID: AB_2750809, A86), mouse monoclonal anti-$Ca_V\beta2$ (1:50, RRID: AB_2750822, A132), rabbit anti-$Ca_V\beta3$ (1:500, RRID: AB_2039787, A20), monoclonal mouse anti-$Ca_V\beta4$ (1:100, RRID: AB_10671176, A123), monoclonal mouse anti-PSD-95 (1: 200, RRID: AB_10698024, A149), guinea pig anti-vGlut1 (1:500, AB_887878, A50), and mouse monoclonal anti-HA (1:250, AB_2565006, A12). After staining with primary antibody, coverslips were rinsed twice and washed 3-4 times for 5 min in TBP. Alexa Fluor 488, 555, and 633 conjugated secondary antibodies were used at 1:500 dilution in TBP. Secondary antibody staining was done for 1 h at room temperature followed by rinsing two times and washing 3-4 times 5 min in TBP. Coverslips were rinsed once with deionized water then mounted on glass slides.

For quantification of synaptic protein levels, neurons were stained with antibodies against MAP2, Synaptophysin, and a target protein of interest. Images were acquired with a 60X oil immersion objective with 1.4 numerical aperture. A ~30 μm x 7.5 μm rectangular section of dendrite was selected for analysis from each image with criteria for selection being a clear separation from other dendrites based on the MAP2 signal. The background was first subtracted using the rolling ball method with a radius of 2 μm. Regions of interest (ROIs) were then defined using Synatophysin puncta, and the average intensity of the protein of interest (in the 488 channel) inside those ROIs was quantified for each image. The number of ROIs was used to calculate the average synapse density for each imaged dendrite.

For quantification of somatic expression levels of rescue proteins (Figures S7F, S7G, and S9G–S9I) neurons were stained with antibodies against HA (rescue protein), PSD-95, and the vesicular marker VGluT. Images were acquired with a 60X oil immersion objective with 1.4 numerical aperture. ROIs were defined by nuclear EGFP fluorescence from EGFP-tagged cre and delta-cre. These ROIs were expanded to encompass the entire cell soma using the somatic background staining of PSD-95. The mean intensity of the HA signal within somatic ROIs was calculated for each image. For Sholl analyses, neurons were patched in whole-cell configuration and filled with intracellular solution containing (in mM) 140 K Gluconate, 0.1 EGTA, 2 $MgCl_2$, 4 Na_2ATP, 1 Na_2GTP, 0.3 Fluo5F, 0.03 Alexa Fluor 594, 10 HEPES-KOH (pH 7.4, ~300 mOsm). After breaking in, the cell was filled for 10 min at an access resistance below 30 MΩ. After filling, the patch pipette was withdrawn, and the coverslip was rinsed once with PBS, followed immediately by fixation with 4% PFA + 4% sucrose (in PBS). Fixed coverslips were mounted on glass slides and imaged via confocal microscopy. Images were acquired with a 40X oil-immersion objective with a 1.3 numerical aperture. Z stacks covering the entire depth of each neuron were acquired, and maximum intensity projections were used for image analysis. Images were thresholded manually to select all visible processes then binarized. Binary images were processed using a closing operation (opening followed by erosion) to connect any thin processes that were broken during thresholding. Binary images were then processed using the Sholl analysis plug-in of ImageJ. Cell somata were selected manually and the number of process crossings of concentric circles originating on the soma at intervals of 10 μm (sholl radius) were counted for each genotype.

All images were acquired on an Olympus FV1000 confocal microscope. The pinhole was set to one airy unit, and identical settings were applied to all samples within an experiment. When necessary, representative images were enhanced for brightness and

contrast to facilitate visual inspection. All such changes were made after analysis and were made identically for all experimental conditions. Except for Sholl analyses, all image acquisition and analyses comparing two or more conditions were done by an experimenter blind to the condition.

Confocal imaging of calyces of Held in brain slices

Mice were anesthetized with isoflurane, perfused transcardially with 10 mL phosphate buffer (PBS) at 4°C and fixed with 10 mL 4% PFA dissolved in PBS at 4°C. After perfusion, the brain was removed and kept in 4% PFA overnight at 4°C. Coronal slices (40 μm) containing MNTB were cut using a vibratome (Leica, VT1000s) in ice-cold PBS. All slices were blocked in 10% goat serum in PBS, permeabilized in 0.25% Triton X-100 in PBS, stained in primary antibodies for 12h at 4°C and secondary antibodies for 2 h at room temperature, and mounted on #1.5 cover glasses. Single-section confocal images were acquired on an Olympus FV1000 confocal microscope with an oil immersion 60X objective, N.A 1.4. The following primary antibodies were used for staining: mouse anti-Bassoon^{N} (N-terminal, 1:500, RRID: AB_11181058, A85), rabbit anti-RIM1 (1:500, RRID: AB_887774, A58), custom-made rabbit anti-ELKS2α (serum E3-1029, 1:500, A136), guinea pig anti-vGlut1 (1:500, RRID: AB_887878, A50). Alexa Fluor 488 and 633 conjugated secondary antibodies were used at 1:500 dilution. Only mCherry positive calyces were used for quantification. ROIs were first defined by the vGluT1 channel using automatic segmentation (Otsu algorithm). The average intensities of RIM and ELKS within the ROIs were then quantified. Bassoon puncta within the ROIs were first recognized using manual thresholding defined by the experimenter on an image-by-image basis before the quantification of intensity and density. Representative images were brightness and contrast adjusted to facilitate inspection, and these adjustments were made identically for images within an experiment. Data acquisition and quantification were done by an experimenter blind to the condition.

Confocal imaging in transfected HEK293T cells

For confocal imaging of $Ca_V2.1$ and α2δ-1 staining in permeabilized HEK293T cells, the cells were plated on Matrigel-coated glass coverslips (12 mm in diameter) at 10%–20% confluency. 24 h later, pCMV-HA-$Ca_V2.1$, pMT2-β1b-GFP and pcDNA-α2δ-1 (1 μg of DNA per coverslip with molar ratio 1:1:1) were transfected into the cells. 36 h after transfection, the cells were fixed and stained as described for neurons. The following primary antibodies were used for staining: mouse monoclonal anti-HA (1:500, RRID: AB_2565006, A12), rabbit anti-α2δ-1 (1:500, RRID: AB_2039785, A133). Alexa Fluor 488- and 555-conjugated secondary antibodies were used at 1:500 dilution in TBP. Confocal images were acquired on an Olympus FV1000 confocal microscope with an oil immersion 60X 1.4 objective. For image analysis, HEK293T cells were randomly selected in $Ca_V2.1$ channel and the edge of each cell was manually outlined based on this fluorescent signal. After that, the signal profiles in both the $Ca_V2.1$ and α2δ-1 channels along the selected cell edge were quantified and cross-correlation analysis was performed.

For surface labeling of α2δ-1 in HEK293T cells, the cells were grown on coverslips and were transfected with pcDNA-CMV-α2δ-1 (0.33 μg/coverslip) and pcDNA-CMV-EYFP (0.033 μg/coverslip) with or without pCMV-HA-$Ca_V2.1$ + pMT2-β1b-GFP (0.67 μg additional DNA per coverslip with molar ratio of 1:1). 36 h later, cells were washed twice using PBS buffer at room temperature. Primary antibodies, mouse monoclonal anti-HA (1:500, RRID: AB_2565006, A12) and rabbit anti-α2δ-1 (1:500, RRID: AB_2039785, A133), diluted in PBS were added directly to the cells and incubated for 60 min at 4°C. After washing twice with PBS at room temperature, the cells were fixed for 10 min using 4% PFA in PBS and stained for 1 h using secondary antibodies coupled to Alexa Fluor 488 or 555 in 3% bovine serum albumin (dissolved in PBS). Coverslips were then mounted on glass slides and imaged on a Leica SP8 confocal microscope with an oil immersion 63X 1.44 numerical aperture objective. For quantification of surface levels of α2δ-1 in HEK cells, an ROI of the EYFP channel was drawn with the ImageJ "Analyze particles" function, the edge of the ROI was considered the cell surface, and the intensity of α2δ-1 on the surface was then quantified. Representative images were brightness and contrast adjusted to facilitate inspection, and these adjustments were made identically for images within an experiment. All image acquisition and analyses comparing two or more conditions were done by an experimenter blind to the condition.

Statistics

Statistical significance was set at * $p < 0.05$, ** $p < 0.01$, and *** $p < 0.001$. For each experiment, the values and definitions of n are specified in the figure legends, followed by the number of cultures, transfections, mice or other relevant replicates. Mann-Whitney rank sum tests were used for Figures 1E, 1G, 1I, 1J, 1L, 1N, 2C, 2F, 5D–5F, 5H–5K, S1J, S1K, S2B, S3B, S3C, S4D, S4N, S5H–S5J, S5L–S5N, and S6P. Because some datasets lacked homoscedasticity, Kruskal-Wallis analysis of variance with post hoc Dunn's test were used for multigroup comparisons in Figures 6M, 7F, 7H, 8E, 8G, S5C, S5D, S6B, S7G, S8E, S8F, S8K, S8L, S9H, and S9I. Two-way ANOVA tests were performed with genotype and position as the two factors for Figures 1C, 2I, 3F–3L, 4C, 4E, 4G, 4I, 6C, 6F, 6I, 7D, 8C, S1H, S2D–S2E, S3E–S3K, S4B, S4F, S4H, S4J, S4L, S4P, S4R, S4F, S4K–S4M, S4R, S7J, S8C, S8I, and S9C–S9F. S4. For statistical analysis of STED side-view profiles, a 100 nm window around the peak was assessed. Paired-t tests were used for Figure S6B. Mann Whitney rank-sum test with post hoc Holm-Sidak test to correct for multiple comparisons for Figures 3M, 3N, and 3P–3R.